



HAL
open science

Wind speed dependence of atmospheric boundary layer optical properties and ocean surface reflectance as observed by airborne backscatter lidar

Cyrille Flamant, Vincent Trouillet, Patrick Chazette, Jacques Pelon

► To cite this version:

Cyrille Flamant, Vincent Trouillet, Patrick Chazette, Jacques Pelon. Wind speed dependence of atmospheric boundary layer optical properties and ocean surface reflectance as observed by airborne backscatter lidar. *Journal of Geophysical Research. Oceans*, 1998, 103 (C11), pp.25137-25158. 10.1029/98JC02284 . hal-02902620

HAL Id: hal-02902620

<https://hal.science/hal-02902620>

Submitted on 20 Jul 2020

HAL is a multi-disciplinary open access archive for the deposit and dissemination of scientific research documents, whether they are published or not. The documents may come from teaching and research institutions in France or abroad, or from public or private research centers.

L'archive ouverte pluridisciplinaire **HAL**, est destinée au dépôt et à la diffusion de documents scientifiques de niveau recherche, publiés ou non, émanant des établissements d'enseignement et de recherche français ou étrangers, des laboratoires publics ou privés.

Wind speed dependence of atmospheric boundary layer optical properties and ocean surface reflectance as observed by airborne backscatter lidar

Cyrille Flamant and Vincent Trouillet

Service d'Aéronomie du Centre National de la Recherche Scientifique, Institut Pierre-Simon-Laplace, Université Pierre et Marie Curie, Paris

Patrick Chazette

Laboratoire des Sciences du Climat et de l'Environnement, Institut Pierre-Simon-Laplace, Gif sur Yvette, France

Jacques Pelon

Service d'Aéronomie du Centre National de la Recherche Scientifique, Institut Pierre-Simon-Laplace, Université Pierre et Marie Curie, Paris

Abstract. Airborne backscatter lidar measurements made over the Azores, in clear air conditions, are analyzed using a marine aerosol model to derive the extinction coefficient in the atmospheric boundary layer and the ocean surface reflectance in connection with surface wind speed. The dependence of surface layer extinction coefficients on surface wind speed is compared to previously published results. The sensitivity of the lidar inversion procedure to the aerosol model (sea-salt concentration in the accumulation mode, presence or absence of an accumulation mode for sulfate, vertical distribution of stationary marine components above the marine atmospheric boundary layer) is investigated. At the wavelength of the lidar ($0.53 \mu\text{m}$), the extinction coefficient is very sensitive to the sea-salt number concentration in the accumulation mode. In the surface layer, the extinction coefficient retrieved from the lidar measurements compares well to the extinction calculated with the model (via Mie theory) for an average number concentration of $10 \text{ particles cm}^{-3}$ in the sea-salt mode at wind speeds less than 3 ms^{-1} . The relationship between the sea surface reflectance and the atmospheric backscatter coefficient is then used to determine the optical sea surface properties as a function of wind speed. Results on reflectance are found in excellent agreement with calculated values using the model of Cox and Munk [1954] and measured wind speed. The sensitivity of the results to the aerosol model and potential application of the inversion procedure to surface wind speed retrievals from lidar measurements are also discussed.

1. Introduction

Aerosols have been shown to have a significant direct and indirect impact on the Earth's radiation budget [Charlson *et al.*, 1992; Fouquart and Isaka, 1992; Intergovernmental Panel on Climate Change (IPCC), 1996]. A better understanding of this impact requires a precise determination of their size distribution, composition, and spatial variability over the globe. This is particularly true on the vertical and over the ocean, where measurements are sparse.

Depending on the size and composition of aerosol, modifications of the microphysical properties of ma-

rine stratiform clouds have been observed [Fouquart and Isaka, 1992]. Inversely, the size and composition of aerosol in the boundary layer have been observed to be modified by in-cloud chemical reactions [Hoppel *et al.*, 1990; Hegg *et al.*, 1993]. Over the open ocean, such processes have been identified as a source of sulfate production [Hegg *et al.*, 1993], which may depend on sea-salt concentration for particle sizes in the micron range [Hegg *et al.*, 1992]. Such aerosol particles, with modal radii comparable to the wavelength of light in the visible spectrum, significantly affect the amount of light transferred into the ocean as well as the light scattered in the lower atmospheric layers, therefore modifying the Earth albedo. Therefore establishing the Earth's energy budget at the regional scale requires the knowledge of the vertical distribution of small-sized sea-salt particles.

Near the surface, sea-salt particles are produced by bubble bursting, which increases as a function of sur-

Copyright 1998 by the American Geophysical Union.

Paper number 98JC02284.
0148-0227/98/98JC-02284\$09.00

face wind speed (SWS) [Blanchard and Woodcock, 1980; Gong et al., 1997]. Relationships have been established between microphysical properties of the sea-salt aerosol and SWS from in situ observations in the marine atmospheric boundary layer (MABL) [Blanchard and Woodcock, 1980; Hoppel et al., 1990; Smith et al., 1989, 1993; Gong et al., 1997]. Average SWS determines the concentration of maritime aerosol in the accumulation mode range [Gathman et al., 1989; Hoppel et al., 1990; Gong et al., 1997]. SWS also affects the sea surface state, modifying the wave slope distribution and, in turn, the energy transfer at the ocean surface. An accurate determination of SWS is therefore of prime importance for the analysis of energy and matter fluxes at the ocean-atmosphere interface and the Earth's energy budget. As the ocean optical surface reflectance is linked to SWS [Cox and Munk, 1954], optical remote sensing is also a very sensitive way to analyze the microphysical properties of aerosol in the micron range [Kaufman et al., 1997]. Spaceborne optical measurements can provide information on both aerosol and SWS characteristics on a large scale. Backscatter lidar measurements have potentially interesting applications in this respect, as they can simultaneously provide MABL parameters, such as average depth [Melfi et al., 1985; Flamant and Pelon, 1996], extinction coefficients [Klett, 1985; Flamant and Pelon, 1996], and sea surface reflectance [Bufton et al., 1983; Menzies et al., 1994], taking into account its ranging capability. Near-surface parameters could then be retrieved from future spaceborne lidar system observations to provide additional information on the atmospheric boundary layer (ABL) and aerosol properties at the ocean-atmosphere interface at the global scale as previously proposed by Weinman [1988] and demonstrated by Winker et al. [1996]. It is the purpose of this paper to investigate, in more detail, the contribution of airborne lidar measurements to this respect, using field campaign data.

During the last 2 decades, backscatter lidar has been used to provide a detailed analysis of the atmospheric scattering layers, namely, for studying scattering properties of aerosols and clouds [Spinhirne et al., 1980; Spinhirne and Hart, 1990; Dupont et al., 1994; Chazette et al., 1995], which are of interest in energy budget studies. Other applications, such as the study of the ocean surface reflectance, have also been developed [Petri, 1977; Bufton et al., 1983; Menzies, 1995]. Lidar systems have been used to study the dynamics of the ABL during cold air outbreaks over the ocean [Melfi et al., 1985; Boers et al., 1990; Flamant and Pelon, 1996] and have recently proven their ability to perform measurements of the aerosol and cloud structure at high vertical resolution from space [Strawbridge and Hoff, 1996; Winker et al., 1996].

Aerosol property analysis by lidar requires the inversion of the lidar signal which, in turn, requires the knowledge of (1) a boundary condition (BC), taken in the form of a reference extinction coefficient (or

backscatter coefficient) value; and (2) the profile of the normalized backscatter phase function (the ratio of the backscatter to the extinction coefficient) of the scatterers. The sensitivity of the retrieved extinction coefficient profile thus needs to be assessed with respect to these input parameters.

For optically thick layers, the reference value has to be taken far from the emission source in order to ensure the stability (reliability) of the solution, as shown by Klett (1981, 1985). However, this requirement is hard to fulfill in the case of airborne (or spaceborne) backscatter lidars operating in a downward looking mode, as the aerosol content near the surface is high and unknown. The lidar surface return can be used to determine a reference near the surface [Weinman, 1988; Reagan and Zielinskie, 1991; Menzies et al., 1994], provided that the SWS is known (or measured separately).

Forward inversion procedures, using an upper level reference, have thus generally been preferred. However, they may lead to unstable solutions if the ratio of the backscatter to the extinction coefficient is not accurately known [Klett, 1981].

In order to increase the contribution of airborne and spaceborne lidar systems to the analysis of atmospheric scattering layers and ocean surface properties, the purpose of this paper is to test an aerosol model suited to forward lidar inversion in the lower atmosphere over the ocean. It is also to analyze (1) the dependence of the retrieved extinction coefficient with respect to SWS and (2) the relationship between the measured ocean surface reflectance and backscatter coefficient in the first tens of meters above the surface. Finally, the purpose of this paper is to determine the sensitivity of the lidar-derived extinction coefficients and sea surface reflectances to the input parameters of the aerosol model.

The analysis of aerosol and surface properties is done using data acquired over the Azores during the Surface Océanique et Flux à l'Interface Atmosphérique (SOFIA) [Weill et al., 1995] and Structure des Echanges Mer-Atmosphère, Propriétés des Hétérogénéité Océanique: Recherche Expérimentale (SEMAPHORE) [Eymard et al., 1996] experiments. SOFIA took place during the Atlantic Stratocumulus Transition Experiment (ASTEX) [Albrecht et al., 1995] in June 1992. SEMAPHORE was held in October and November 1993. During these campaigns, the French airborne backscatter lidar LEANDRE 1 was flown on board the French Avion de Recherche Atmosphérique et de Télédétection (ARAT).

MABL models have been developed to determine aerosol optical properties as a function of meteorological conditions [Fairall et al., 1984; De Leeuw, 1989; Gathman et al., 1989]. In this paper, different parameterizations have been used. The vertical distribution of sea-salt concentration is modeled as a function of SWS, according to the work of Blanchard and Woodcock [1980], Exton et al. [1985], and Smith et al. [1989, 1993]. Sulfate concentrations, prescribed as a function

of the origin of the air mass and its time of travel over the ocean, are based on the work of *Gathman* [1983] and on measurements made over the Atlantic [*Hoppel et al.*, 1990; *Hegg et al.*, 1993]. Finally, hygroscopic properties of sulfate and sea-salt aerosols are modeled according to the work of *Hänel* [1976] and *Fitzgerald et al.* [1982]. The aerosol model is presented in section 2. In section 3, normalized backscatter phase function profiles are derived from the aerosol model for both experiments. Errors related to the relative humidity and SWS variability and biases inherent in the aerosol model are discussed. In section 4, we discuss the surface layer extinction coefficients obtained with the lidar inversion procedure as well as the related errors. In section 5, the relationship between the measured ocean surface reflectance and backscatter coefficient in the first tens of meters above the surface is used to compare the calculated reflectances with those obtained from the model of *Cox and Munk* [1954]. The estimate of SWS is then discussed. Results are summarized and discussed in the last section.

2. Aerosol Model

Over the open ocean, the aerosol population consists essentially of ammonium sulfate and sea-salt particles. Volcano and desert aerosols are not accounted for in this model because, in this study, we only consider cases where these aerosols were not advected over the experimental area. Although an exhaustive sensitivity analysis of the extinction and sea surface reflectance to the model is beyond the scope of this paper, we have focused on the critical parameters of this aerosol model (number concentration, vertical distribution, relative humidity effects, aerosol composition) with respect to lidar measurement analysis. In the following sections, detailed discussions on the errors and biases associated with the aerosol models for extinction and reflectance retrievals from lidar measurements are provided. By "bias" we mean the difference between two values of given parameter retrieved using the aerosol model for different sets of input parameters. By "error" we mean the error on a given parameter, derived for a given set of model inputs, resulting from the uncertainties on measurements acquired in the framework of the SOFIA and SEMAPHORE experiments.

The concentration of sea-salt particles is strongly dependent on the surface wind speed [*Blanchard and Woodcock*, 1980; *Exton et al.*, 1985; *Smith et al.*, 1989, 1993]. The particle size distributions previously measured by in situ means show the existence of two sulfate modes [*Hoppel et al.*, 1990; *Hegg et al.*, 1993; *Jaenicke*, 1993; *Kim et al.*, 1995; *O'Dowd et al.*, 1997] and up to three sea-salt modes [*Smith et al.*, 1989, 1993].

The smaller sulfate mode corresponding to the nucleation process is found around $0.028 \mu\text{m}$. In the clean MABL, it relates to sulfate originating from dimethylsulfide (DMS) gas-to-particle conversion [*Russel et al.*,

1994]. The second sulfate mode is found around $0.133 \mu\text{m}$ and is related to sulfate processing by clouds [*Hoppel et al.*, 1990; *Hegg et al.*, 1993; *Kim et al.*, 1995; *O'Dowd et al.*, 1997]. In air masses of continental origin, *Hoppel et al.* [1990] have observed large number concentrations of small sulfates (around $0.028 \mu\text{m}$) just off the east coast.

An accumulation mode of aged (stationary) marine particles is observed around $0.3 \mu\text{m}$ [*Shettle and Fenn*, 1979; *Jaenicke*, 1993], which consist essentially of sea-salt aerosols. A mode centered around $2 \mu\text{m}$ is associated with freshly produced sea-salt aerosols generated by both surface tearing and bubble-mediated production [*Gathman*, 1983; *Smith et al.*, 1989]. At wind speeds larger than 13 m s^{-1} , large-sized sea-salt aerosols result from the contributions of sea spray aerosol (spume drops). They are observed to present enhanced concentrations for radii around $9 \mu\text{m}$ and above [*Smith et al.*, 1989, 1993]. However, in this study, we did not attempt to account for such large particles (as further discussed in section 2.2). For the remainder of this paper, units for concentrations are particles per cubic meter, unless noted otherwise.

2.1. Ammonium Sulfate Aerosol Modeling

Over the ocean, the sulfate particle content depends on the type of air mass and its history. Therefore continental influence, cloud cover, and time of residence of the air mass over the ocean are the parameters relevant to our study.

The back trajectories of the 11 air masses sampled by lidar over the course of the SOFIA and SEMAPHORE experiments were calculated using a zoom version of the global atmospheric tracer model TM2 [*Heinmann*, 1995] initially developed at the Max Plank Institut für Meteorologie, Hamburg, Germany. This zoom version, TM2Z [*Ramonet and Monfray*, 1996], has a 2.5° by 2.5° horizontal resolution and uses the three-dimensional wind field analysis of the European Center for Medium-Range Weather Forecast (ECMWF) data assimilation system.

Data from SOFIA/ASTEX were acquired throughout the month of June. During the 5 days considered in this study, a high-pressure system was located over the Azores, leading to back trajectories from the east. On June 1, 1992, June 8, 1992 and June 9, 1992, 6-day back trajectories are from the northern continental United States. On June 4, 1992 and June 26, 1992, 6-day back trajectories are from the open northern Atlantic (Figure 1). Data from SEMAPHORE were acquired in a short period of time (6 days) in air masses of similar origin. Prevailing winds were from the northeast, as a low-pressure center passed over the experimental zone [*Eymard et al.*, 1996]. This led to low-level north easterly back trajectories from Europe from October 13, 1993 (Figure 1) to October, 17 1993.

Since back trajectories for SOFIA indicate that the air masses originated from the U.S. continent, we have used in situ measurements made by *Hoppel et al.* [1990] to estimate the total sulfate concentration. These mea-

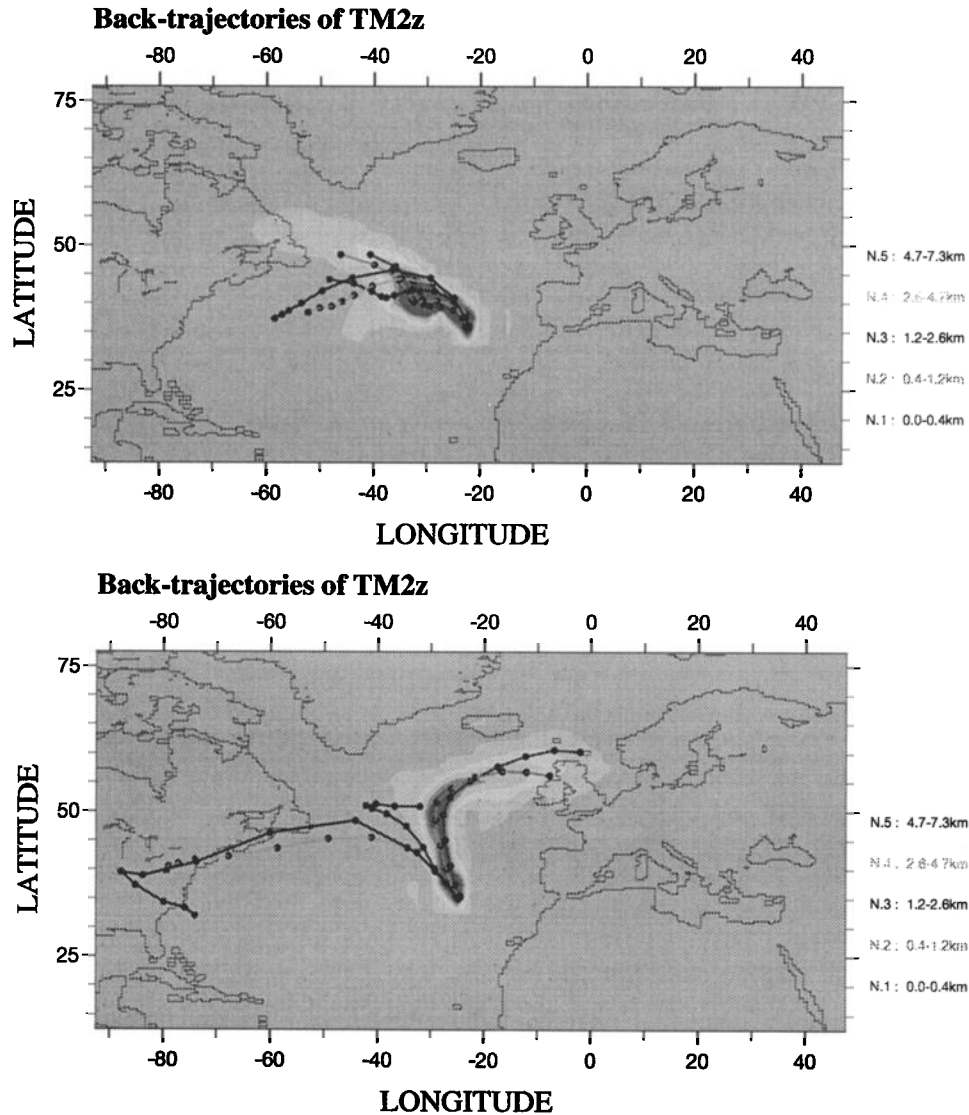


Figure 1. Global atmospheric tracer model, zoom version (TM2Z) 6-day back trajectories of the air masses sampled over the Azores during (top) Surface Océanique et Flux à l'Interface Atmosphérique (SOFIA) on June 4, 1992 and (bottom) Structure des Échanges Mer-Atmosphère, Propriétés des Hétérogénéité Océanique: Recherche Expérimentale (SEMAPHORE) on October 13, 1993. Dots are separated by 12 hours. SWS is surface wind speed.

measurements reveal aerosol contents as high as 1920 particles cm^{-3} for air masses having spent less than 18 hours above the ocean. This concentration has been observed to decrease to 1325 particles cm^{-3} for air masses 60 hours above the ocean and 200 particles cm^{-3} for the background Atlantic Ocean conditions (away from any continental influence). The size distribution spectrum gradually changes from single peaked (short residence time over the ocean) to double peaked (background conditions), stressing the importance of sulfate processing by clouds in the generally cloud topped MABL.

In our study, we have assumed sulfate concentration to decrease from a continental value to an open ocean value, as a function of the time traveled by the air masses above the ocean [Gathman, 1983]. Air masses on all 11 days traveled at least 5 days over the ocean be-

fore reaching the region of the experiment. In the worst case scenario, the air mass would originate from the US or European continent and reach the Azores in 5 days. According to Gathman [1983], the sulfate concentration would have, in the mean time, decayed to about 300 particles cm^{-3} . Therefore sulfate concentration is expected to range between the background Atlantic sulfate concentration and 300 particles cm^{-3} during SOFIA, which means that we can neglect the influence of continental sulfates in this study, only to consider the processes relevant to sulfate production in open ocean conditions, namely, DMS and cloud processing.

However, there might exist an additional uncertainty on the sulfate content estimated during SEMAPHORE because our calculations are based on measurements made off the U.S. east coast rather than the north-

ern Atlantic Ocean west of the British Isles. We also have accounted for the uncertainty associated with the exact location of an air mass while tracking its origin. For TM2Z, it is on the order of 300 km beyond 4 days. Overall, for both SOFIA and SEMAPHORE, the sulfate content is expected to range between the background Atlantic sulfate concentration and 350 particles cm^{-3} . In the following sections, the uncertainty on this value is used to estimate the error associated with the aerosol model.

Lidar signal depends on the aerosol extinction and backscatter cross section as well as particle number concentration. The measurements analyzed here were taken at a wavelength of 0.532 μm . In the visible, the backscatter efficiency of particles of radius smaller than 0.05 μm is not significantly different from the backscatter efficiency of molecules. However, the nucleation mode, having the largest magnitude and being the broadest, extends beyond 0.1 μm , and we did not discard its contribution to the total extinction.

2.2. Sea-Salt Aerosol Modeling

Using the particle distribution observed near the surface by *Smith et al.* [1989], at SWS of 10 m s^{-1} , we have calculated the relative contribution of the three sea-salt modes to the total sea-salt related extinction at 0.532 μm . The 2 and 9 μm modes were found to contribute 1% and 0.5%, respectively. With these values being much smaller than the uncertainty on the lidar derived extinction coefficients (see section 4.1), we thus neglected contributions of the 2 and 9 μm modes to the surface layer extinction derived from lidar. Moreover, large particles have higher deposition velocities than particles in the 0.1–0.5 μm range [*Smith et al.*, 1989]. The deposition velocity also increases with wind speed so that even for high wind speeds (strong turbulence regime), particles with radii larger than 1 μm are hardly ever observed above the surface layer [*Park et al.*, 1990]. The fraction of sea salt whose size exceeds 1 μm has been measured to decrease rapidly in the first 100 m above the oceanic surface [*Park et al.*, 1990]. Measurements by *Park et al.* [1990] show that the number of particles of size ranging from 1.5 to 10 μm is roughly 1 out of 40,000 in the surface layer and less above it.

The vertical distribution of aerosol extinction in the ABL results from production, sedimentation, accumulation, and mixing processes [*Fairall et al.*, 1984, *Jaenicke*, 1993] which are characterized by different timescales. Aerosol properties observed by lidar should exhibit a strong correlation with the average wind (rather than the instantaneous wind), as the accumulation mode consists of particles that, given their size (close to the laser wavelength), interact with and scatter the laser light more efficiently than those present in the other modes. As a result, since we neglect the contribution of freshly produced sea-salt aerosol and only keep the aged aerosol contribution, the notion of time-averaged

wind [*Hoppel et al.*, 1990; *Gong et al.*, 1997] is used throughout this paper when referring to the SWS used in the aerosol model. The abbreviation ASWS is used in the text, and the expression \bar{U} is used in equations. \bar{U} designates the mean wind speed at (or close to) 10 m, unless noted otherwise.

Figure 2 is a schematic representation of the modeled sea-salt distribution, both as a function of height and surface wind speed. On the basis of in situ measurements of *Blanchard and Woodcock* [1980], *Exton et al.* [1985] and *Smith et al.* [1989], sea-salt concentration in the surface layer N_{se} is modeled as

$$\begin{cases} N_{se} = N_{se0}, & \bar{U} \leq 3 \text{ m s}^{-1}; \\ N_{se} = N_{se0} [1 + 0.5(\bar{U} - 3)], & \bar{U} \leq 10 \text{ m s}^{-1}; \\ N_{se} = 4.5 N_{se0} (\bar{U}/10)^3, & \bar{U} \leq 15 \text{ m s}^{-1}. \end{cases} \quad (1)$$

Since no bubbles are produced by the sea at wind speeds less than 3 m s^{-1} [*Blanchard and Woodcock*, 1980], the sea-salt concentration N_{se0} is taken to be independent of wind speed. N_{se0} accounts only for the aged aerosols (accumulation mode) resulting from at least 12 hours of wind speeds in the 0–3 m s^{-1} range. Values of N_{se0} between 4 and 14 particles cm^{-3} have been deduced from in situ measurements by *Blanchard and Woodcock* [1980], *Jaenicke* [1993], and *O'Dowd et al.* [1997], among others. Sea-salt concentration is modeled as increasing linearly with wind speed between 3 and 10 m s^{-1} . At wind speeds greater than 10 m s^{-1} , sea-salt concentration is supposed to increase with the third power of wind speed [*Blanchard and Woodcock*, 1980].

As we kept only the aged (small) sea salts in our model, their concentration in the mixed layer is assumed to be independent of height [*Monahan et al.*,

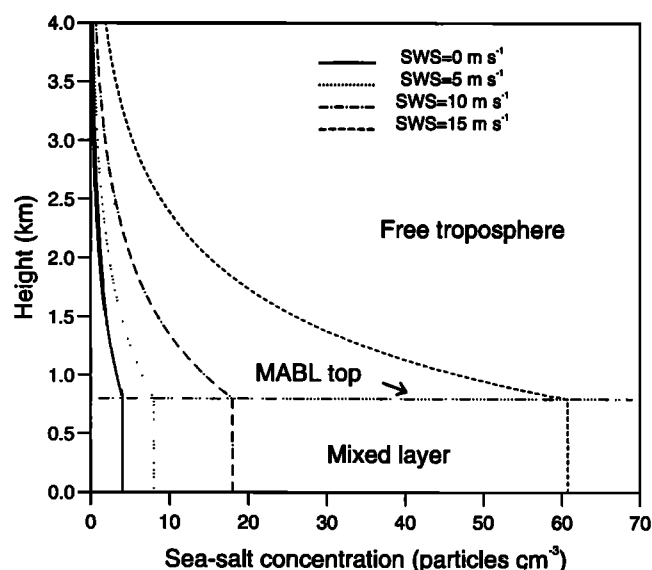


Figure 2. Schematic representation of sea-salt aerosol concentration distribution as a function of surface wind speed and height. Results are based on the model provided by equations (1) and (2).

1986]. Uniform mixing of aged aerosols in the mixed layer is to be expected since lighter particles are good tracers of the MABL dynamics. This has been observed by *Blanchard and Woodcock* [1980] for low and intermediate wind regimes (defined as ASWS ranging from 3 to 13 ms^{-1}). Blanchard and Woodcock's concentration measurements (given in micrograms per cubic meter) decrease linearly with height in the mixed layer. However, in terms of particles per cubic meter, sea-salt concentrations remain nearly constant in the mixed layer.

Because of the increasing stability and sedimentation effects, the sea-salt concentration decreases to nearly zero above the mixed layer. According to *Jaenicke* [1993], we used an exponential decay to represent the average concentration:

$$N_{se} = N_{se0} \exp[-(z - \bar{h})/H] \quad (2)$$

where \bar{h} is the depth of the MABL and H is a height scale. Using in situ measurements shown by *Blanchard and Woodcock* [1980] and *Blanchard et al.* [1984], we have estimated H to range between 0.5 and 2 km. This point is further discussed in section 2.3.

2.3. Sea-Salt/Sulfate Aerosol Mixture in Open Ocean Conditions

We have considered a trimodal size distribution (sulfate particles for the two smaller radius modes and aged sea-salt aerosols for the larger one) as representative of the scatterer population interacting with the laser beam in the boundary layer over the open ocean. Nucleation and accumulation modes size spectra are described by lognormal distributions in our model. The corresponding mode radii (reported in Table 1) are 0.0285, 0.133, and 0.3 μm , with dispersions of 2.24, 1.6, and 2.51 μm , respectively [*Shettle and Fenn*, 1979; *Jaenicke*, 1993]. The extreme modes are similar to those used in the Navy Aerosol Model (NAM) [*Gathman*, 1983] and located at 0.03 and 0.24 μm . The standard deviation of the lognormal sea-salt distribution is assumed independent of wind speed (as in NAM). Justification for this

assumption can be found in the measurements of *Hoppel et al.* [1990] over a 35-hour period for wind speed ranging from 1 to 7 ms^{-1} . Their size distributions (about 50 overall, away from any continental influence) indicate that the change in dispersion for the two sulfate modes is of the order of the measurement uncertainty.

As mentioned before, the extinction retrieved from lidar measurements is sensitive to the number of particles in the cloud-processed sulfate and sea-salt modes. Since there exists a large uncertainty in the cloud cover experienced by the air masses sampled by lidar over the Azores, we have considered two types of aerosol distribution which are summarized in Table 1. We first assumed the MABL aerosols to have experienced cloud processing for at least 5 days (model I) and took 135, 65, and 10 particles cm^{-3} for the sulfate nucleation, sulfate processing by clouds, and sea-salt accumulation modes [*Hoppel et al.*, 1990; *Hegg et al.*, 1993; *Jaenicke*, 1993]. In a second model, we assumed the interaction with cloud cover to be very small and the sulfate concentration in the intermediate mode to be insignificant [*Gathman*, 1983]. We set the concentration of the three modes to 200, 0, and 10 particles cm^{-3} (model II).

The aerosol mixture size distributions modeled using the parameters described in Table 1 are reported in Figure 3 for a relative humidity (RH) of 60%. The effect of RH on the aerosol mixture size distributions needs to be accounted for, as it leads to important variations in the radius of the particles.

2.4. Humidity Effects

As sulfate and sea-salt aerosols are hygroscopic, their radius r_s will increase and their refractive index n_s will decrease with increasing relative humidity. Above critical values of 75% and 81% (corresponding to the deliquescence point of sea salt and ammonium sulfate, respectively), particle growth is enhanced as water vapor condenses on their surface. Following *Hänel* [1976], the particle radii and refractive index for both species were modeled as a function of the relative humidity according to

Table 1. Sulfate and Sea-Salt Aerosol Characteristics in the Surface Layer Used in the Two-Mode Size Distributions

Type of Aerosol	Mode	Aerosol Characteristics			
		Radius r , μm	Dispersion σ , μm	Concentration N_0 , particles cm^{-3}	Dry refractive index n_{s0}
<i>Model I</i>					
sulfate	nucleation	0.0285	2.24	135	$1.53-j 5 \times 10^{-4}$
sulfate	accumulation	0.133	1.60	65	$1.53-j 5 \times 10^{-4}$
sea-salt	accumulation	0.3	2.51	10	$1.38-j 1.1 \times 10^{-6}$
<i>Model II</i>					
sulfate	nucleation	0.0285	2.24	200	$1.53-j 5 \times 10^{-4}$
sea-salt	accumulation	0.3	2.51	10	$1.38-j 1.1 \times 10^{-6}$

Here j denote the imaginary part of the refractive index.

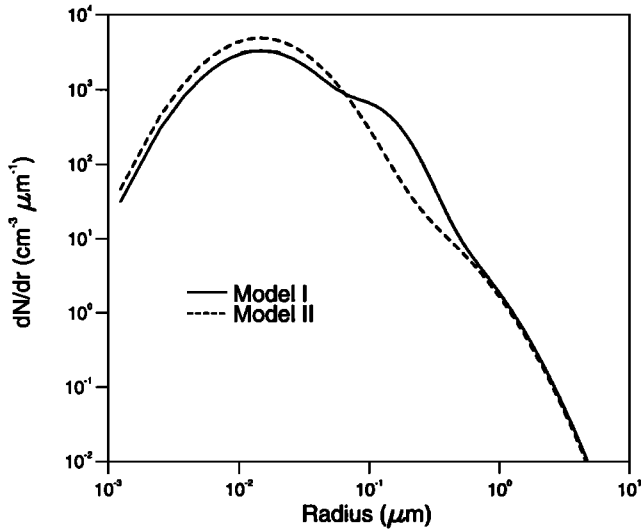


Figure 3. Aerosol size distribution modeled in conditions of open ocean in the marine atmospheric boundary layer (MABL). The solid and dashed lines correspond to aerosol models I and II, respectively of Table 1. Modeled distributions are calculated for a relative humidity of 60%.

$$r_s = r_{s0} (1 - RH)^{-e}, \quad (3)$$

$$n_s = n_{h_2o} + (n_{s0} + n_{h_2o}) (r_s/r_{s0})^{-3}, \quad (4)$$

where subscript s refers to either sulfate or sea salt; r_{s0} and n_{s0} are the radius and refractive index of aerosol particles in dry air, respectively; n_{h_2o} is the water refractive index (equal to 1.33); and e is an exhibitor which depends on the type of aerosol considered. Here e is taken equal to 0.25 for marine aerosols [Shettle and Fenn, 1979]. Equation (3) is valid for values of r_s ranging from 0 to 99%.

Figures 4a and 4b represent the evolution of modal radius and refractive index of sulfate and sea-salt particles as a function of relative humidity as given by the model. The radius increases by a factor of 2 with RH ranging from 80% to 99%. The inverse behavior is observed for the refractive index, as it tends towards the value of the water refractive index at high humidity. The relative variation for sulfate is larger than for sea salt, as the sulfate dry index is much higher than the water index.

Relative humidity soundings from aircraft are used to model the vertical structure of the particle radii and refractive index as a function of height. Mie theory then enables us to calculate the aerosol backscattering phase function as a function of altitude.

3. Dermination of the Parameters Essential to a Lidar Equation Inversion Procedure

For a monostatic and monochromatic lidar, the power collected by the telescope from a given layer of the atmosphere can be related to the backscatter coefficients

of molecules and particles in this layer and the atmospheric transmittance between the laser source and the considered layer (see Appendix A). Solving the lidar equation requires the knowledge of (1) a boundary condition, taken in the form of a reference backscatter coefficient value; and (2) the profile of the ratio of the backscatter coefficient to the extinction coefficient (see (A5)). Whenever the BC is taken closest to the source (the lidar), the solution is referred to as unstable (or forward, the resulting backscatter profile is very sensitive to the initial guess on the BC), whereas if the BC is taken at the far end of the domain, the solution is referred to as stable (or backward, the resulting backscatter profile is fairly insensitive to the initial guess in the BC). For an optically thin lower troposphere (optical depth less than 0.2), the backscatter profile retrieved with the unstable solution is not too sensitive to small uncertainties on the BC value and on the normalized backscatter phase function profile, so that the stable and unstable solution yield the same backscatter profile. For optical depths larger than 0.2, the forward procedure is not reliable unless the normalized backscatter

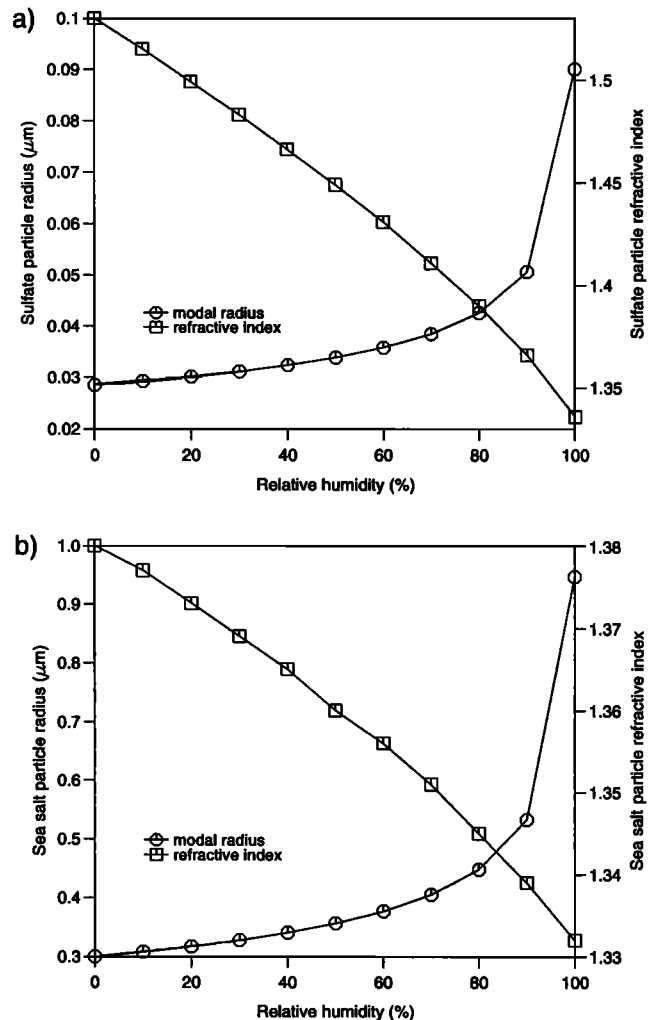


Figure 4. Evolution of the modal radius and the refractive index of particles with relative humidity for (a) sulfate particles and (b) sea-salt particles.

phase function profile is precisely known. In the case of airborne nadir lidar measurements, the unstable solution has generally been used because measurements of the BC at the far end of the domain (the surface of the ocean) are difficult to make simultaneously with lidar measurements, whereas the onboard nephelometer, for example, can provide measurements of the BC near the aircraft.

In this section, we first determine the normalized backscatter phase function using the aerosol model (described in section 2) and analyze the impact of relative humidity. Then, we introduce the BC for the lidar equation inversion procedure.

3.1. Normalized Backscatter Phase Function

The atmospheric extinction coefficient α and backscatter coefficient β are the sum of the contributions of both Rayleigh scattering and absorption by molecules (α_m , β_m) and Mie scattering and absorption by the particles (α_p , β_p) present in the atmosphere. We write

$$\beta(\lambda, z) = \beta_p(\lambda, z) + \beta_m(\lambda, z), \quad (5a)$$

$$\alpha(\lambda, z) = \alpha_p(\lambda, z) + \alpha_m(\lambda, z), \quad (5b)$$

where λ is wavelength and z altitude. Since we consider here measurements taken in the visible, the absorption can be considered as negligible. Indeed, the imaginary part of the refractive index of sulfate and sea-salt is equal to $5 \cdot 10^{-4}$ and $1.1 \cdot 10^{-6}$, respectively [Shettle and Fenn, 1979]. The particle normalized backscatter phase function ϕ_p is then defined by the ratio of the total particle backscatter to extinction coefficients

$$\phi_p(\lambda, z) = \frac{\beta_p(\lambda, z)}{\alpha_p(\lambda, z)}, \quad (6)$$

The same formulation applies to molecular scattering, but in this case the normalized backscatter phase function is constant and equal to $3/8\pi$. The mixing of sulfate and sea-salt aerosols leads to an equivalent normalized backscatter phase function given by

$$\phi_p(\lambda, z) = \frac{\sum_i f^i \beta_p^i}{\sum_i f^i \alpha_p^i}, \quad \sum_i f^i = 1, \quad (7)$$

where f^i represents the fraction of aerosol in mode i .

3.1.1. Normalized backscatter phase function dependence on sea-salt fraction. The most important parameter for lidar inversion is the backscatter to extinction ratio as a function of height. Rather than the number concentrations of each aerosol species, the crucial parameter is the fraction of sea salt in the accumulation mode with respect to sulfate. Mie computation of the aerosol optical properties was carried out in the visible, at $0.532 \mu\text{m}$, which corresponds to the emission wavelength of the lidar. The dependence of ϕ_p on the sea-salt fraction given by (7) is illustrated in Figure 5. The value of ϕ_p is most sensitive to small values of the sea-salt fraction. However, it changes by less than 5% for fractions greater than 24% (model I)

and 4% (model II). If the sea-salt and sulfate number concentrations are not constant with altitude, the sea-salt fraction is changed and the normalized backscatter phase function is modified as shown in Figure 5.

The area between the two curves represents the domain of variation of the normalized backscatter phase function for a cloud processing efficiency (CPE) ranging from 0% (model II) to 33% (model I) (the smaller sulfate particles are processed and return as large ones). The bias introduced on the normalized backscatter phase function by the lack of knowledge of the CPE is larger for small of sea-salt fractions. It is about 1% per percent of CPE at a sea-salt fraction of 1%, and only 0.3% per percent of CPE at a sea-salt fraction of 10%.

We note that for a given model the uncertainty on ϕ_p will be maximum for small values of ASWS (small sea-salt number concentration) and large values of sulfate concentration because these conditions lead to small values of the sea-salt fraction. We have estimated the error on ϕ_p introduced by an uncertainty of 1 ms^{-1} on the measurement of ASWS and the uncertainty on the total sulfate concentration. Assuming a total sulfate concentration typical of background Atlantic Ocean conditions ($200 \text{ particles cm}^{-3}$ in both models), the ASWS corresponding to a given sea-salt fraction can be calculated from (1). Similarly, assuming a sea-salt concentration of $10 \text{ particles cm}^{-3}$, the sulfate concentration can be deduced from the knowledge of the sea-salt fraction.

We took ASWS values ranging from 3 to 5 ms^{-1} and sulfate concentrations between the background Atlantic

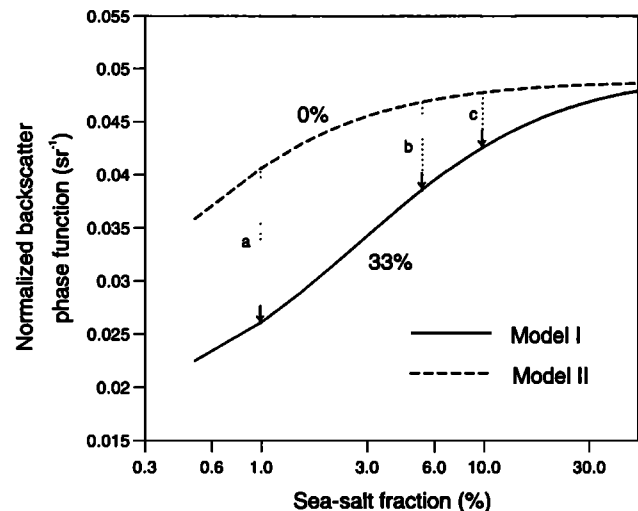


Figure 5. Evolution of normalized backscatter phase function as a function of sea-salt fraction for the two aerosol size distributions shown in Figure 3. Area between the two curves represents the domain of variation of the normalized backscatter phase function for a cloud-processing efficiency ranging from 0% (model II) to 33% (model I) (the smaller sulfate particles are processed and return as large ones). The dotted lines illustrate how the normalized backscatter phase function is affected by cloud processing for sea-salt fractions of 1%, 5% and 10% (dotted lines labeled a, b and c, respectively).

concentration and $350 \text{ particles cm}^{-3}$. The error related to the uncertainty on the sulfate concentration is about 12% for model I and 2% for model II. The difference is mainly due to the sulfate contribution in the accumulation mode. A 1 ms^{-1} uncertainty on ASWS in the low wind speed regime leads to an error smaller than 6% for model I and smaller than 2% for model II. These errors, however, are smaller than the uncertainty associated with CPE (33% for a sea-salt fraction of 1%).

In section 4, these errors and biases on the normalized backscatter phase function will be used to estimate the error on the extinction coefficient retrieved with the lidar inversion procedure.

3.1.2. Normalized backscatter phase function dependence on relative humidity. As humidity increases, the normalized backscatter phase function becomes smaller because of the decreasing refractive index (Figures 4a and 4b). On the other hand, the growth of the particle size with RH forces the phase function to increase. The later effect becomes dominant above 90% RH, so that, at a given wind speed, the normalized backscatter phase function is observed to decrease between 0 and 90% and increase above 90%. This dependence of the normalized backscatter phase function on relative humidity and wind speed in the surface layer is shown on Figure 6. Since all results will be normalized to a RH of 60% in the rest of this study, we have calculated the error on ϕ_p associated with a 10% uncertainty on the measurement of RH at 60%. It is equal to 2% for model I and 1% for model II.

3.1.3. Vertical structure of the MABL as observed by lidar. The MABL structure during flight 27 of SOFIA and flight 34 of SEMAPHORE is illustrated using potential temperature soundings and lidar profiles. The mixed layer lies between the surface and

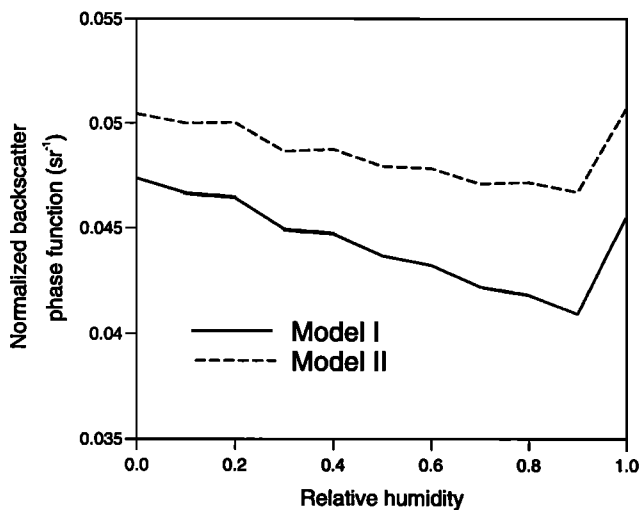


Figure 6. Evolution of normalized backscatter phase function in the MABL as a function of relative humidity for the two aerosol size distributions shown in Figure 3. The surface wind speed is equal to 16 ms^{-1} , which corresponds to the average value measured during the 11 days considered in this study.

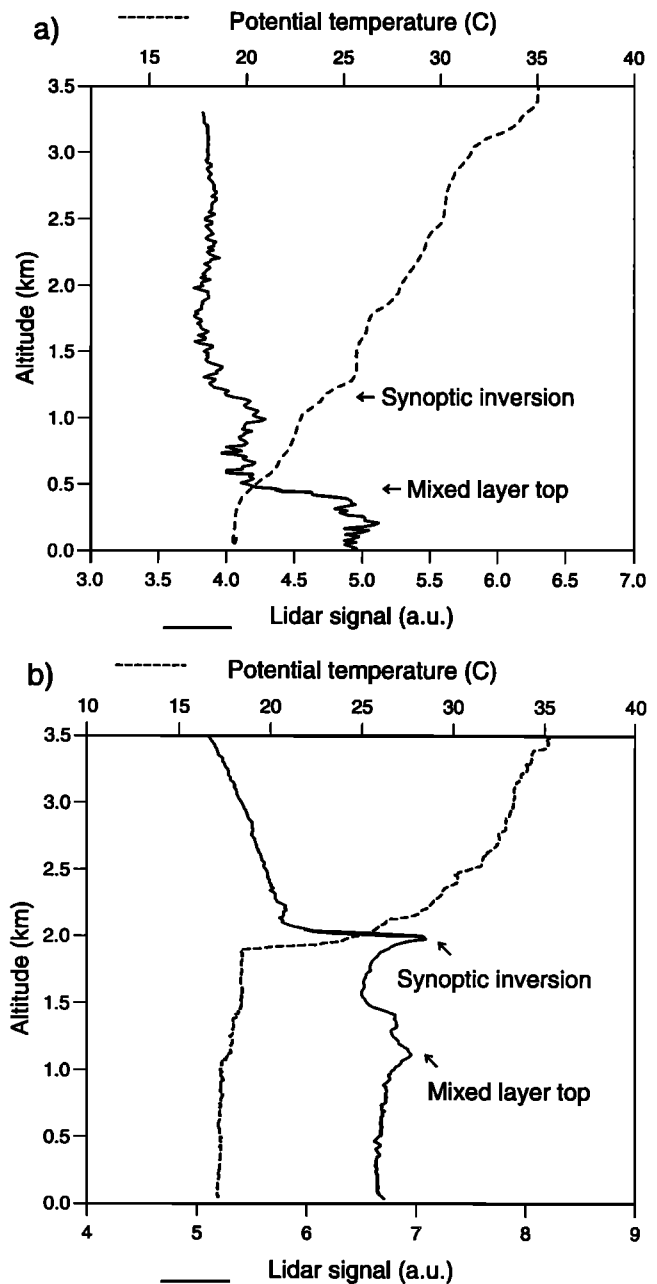


Figure 7. The MABL structure during (a) flight 27 of SOFIA and (b) flight 34 of SEMAPHORE as observed from lidar and potential temperature measurements (solid and dashed lines, respectively). The mixed layer lies between the surface and the first temperature inversion. These weak temperature inversions were observed near 450 m for SOFIA and 1000 m for SEMAPHORE. The synoptic inversion associated with trade winds is observed at altitudes of 1300 and 2000 m for SOFIA and SEMAPHORE, respectively.

the first temperature inversion. This temperature inversion observed on the soundings near 450 m for flight 27 and 1000 m for flight 34 corroborates with the top of the mixed layer height observed on the lidar measurements (Figure 7). The synoptic inversion associated with trade winds is observed at altitudes of 1300 and 2000 m for flights 27 and 34, respectively.

The inversion at the top of the mixed layer prohibits most exchanges of material between the mixed layer and above. However, when the temperature inversion at the top of the mixed layer is weak, as is the case on the profile shown in Figure 7 for SEMAPHORE, the mixed layer and the upper subcloud layer (extending from the top of the mixed layer to the synoptic inversion) are not entirely decoupled. Sea spray aerosol can be transported across the inversion. These exchanges through the inversion are further reinforced by the formation of cumulus clouds at the top of the mixed layer.

This leads us not to take an aerosol number concentration of zero above the mixed layer but, rather, an exponential decay as proposed in the literature. Common sense suggests that the height scale H in (2) is inversely proportional to the inversion strength: a weaker temperature inversion enables convective updraft to penetrate higher in the subcloud layer and to deposit aerosol over greater distances above the mixed layer top. We chose a value of $H = 2$ km (section 2.2) to account for the fairly weak inversion and the difference of altitude between the top of the mixed layer and the synoptic inversion. The sensitivity of the model to the value of H is tested in section 4.2.

3.1.4. Normalized backscatter phase function profile. Figures 8a and 8b show the mean normalized backscatter phase function profile, $\overline{\phi_p}$, and its dispersion (1 standard deviation) during SOFIA (five cases) and SEMAPHORE (six cases), respectively. The mean normalized backscatter phase function profiles are calculated using ship measurements of the ASWS made by *Le Suroit*, humidity profiles (also shown in Figure 8) measured by the aircraft, as well as the vertical distribution of aerosol number concentration parameterized in models I or II. Values of these parameters at 10 m are reported in Table 2. The greater dispersion observed around the phase function profile retrieved with model I is caused by the greater sensitivity of the normalized backscatter phase function with respect to uncertainties in the sea-salt fraction (Figure 5).

During SOFIA, $\overline{\phi_p}$ is almost constant in the mixed layer. Below the synoptic inversion (1.5 km) and above the mixed layer, the dispersion on $\overline{\phi_p}$ is relatively small (less than 5%). In the free troposphere (above the synoptic inversion), RH decreases smoothly to 30% (Figure 8a) while $\overline{\phi_p}$ decreases to a value of about 0.025 sr^{-1} at 4 km. For a RH of 30%, the $\overline{\phi_p}$ related to nucleation sulfate only is equal to 0.021 sr^{-1} , meaning that $\overline{\phi_p}$ is

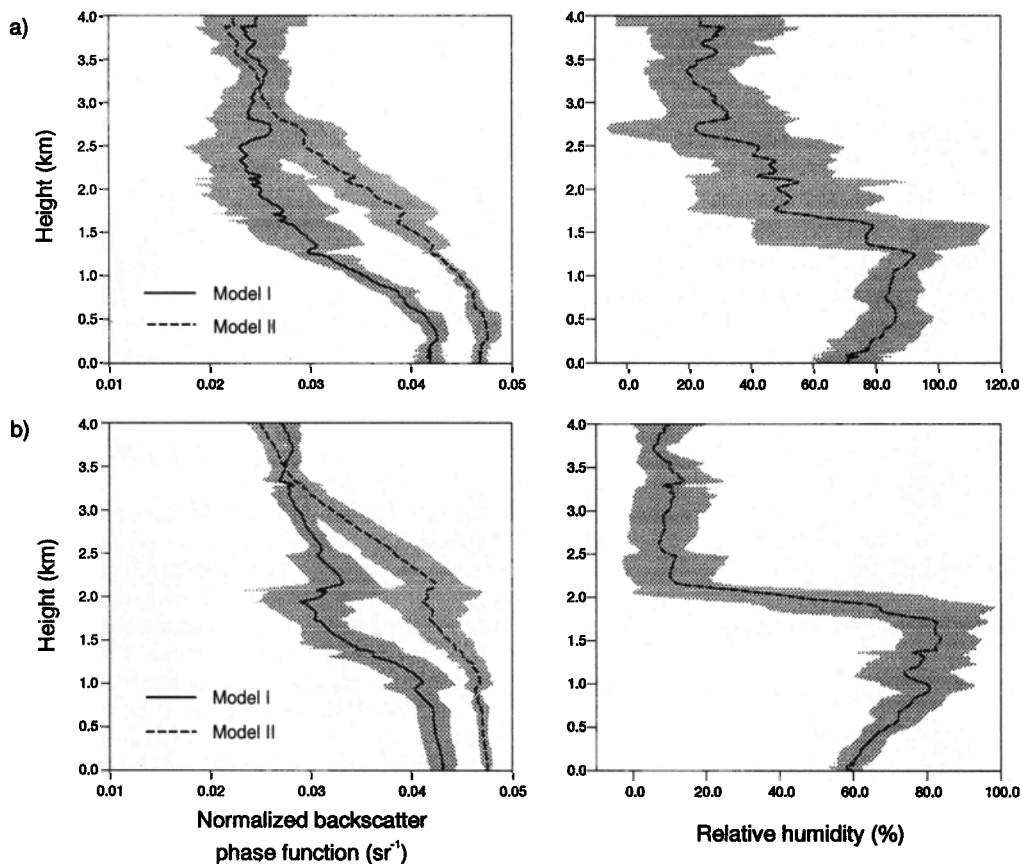


Figure 8. Vertical profiles of both particle normalized backscatter phase function and relative humidity during (a) SOFIA-ASTEX and (b) SEMAPHORE. Data from five flights and six flights are averaged for SOFIA and SEMAPHORE, respectively. Error bars are related to the observed variabilities of the relative humidity profile and surface wind speed. Results are presented for model I (solid line) and model II (dashed line).

Table 2. Flight Average Values of the Mean Surface Wind Speed (ASWS), Relative Humidity (RH), Sea-Salt Fraction f_{ss} , and Normalized Backscatter Phase Function in the Surface Layer $\overline{\phi_p}$

Flight Number	Date	ASWS, m s ⁻¹	RH, %	f_{ss} , %	$\overline{\phi_p}$, sr ⁻¹	
					Model I	Model II
<i>SOFIA</i>						
05	June 1, 1992	6.0	80	12.5	0.042	0.047
09	June 4, 1992	5.1	86	10.0	0.039	0.046
11	June 8, 1992	6.0	65	12.5	0.043	0.048
13	June 9, 1992	4.1	67	7.5	0.041	0.046
27	June 26, 1992	7.0	70	15.0	0.043	0.047
<i>SEMAPHORE</i>						
30	Oct. 13, 1993	6.1	55	12.5	0.044	0.048
31	Oct. 14, 1993	4.1	59	7.5	0.041	0.047
32	Oct. 15, 1993	10.0	66	22.5	0.040	0.047
33	Oct. 16, 1993	5.0	61	10.0	0.042	0.048
34	Oct. 17, 1993	7.1	60	15.0	0.044	0.048
35	Oct. 17, 1993	8.1	62	17.5	0.044	0.048

not affected by the sea-salt population present at that height. Below 3.5 km, the difference in $\overline{\phi_p}$ retrieved with models I and II results from the presence of cloud-processed sulfates. Indeed, the backscatter efficiency of accumulation sulfate particles is much smaller than its extinction efficiency, thus reducing the value of the total mean normalized backscatter phase function. Above 3.5 km, this effect becomes insignificant because both sea salts and cloud-processed sulfates are found in negligible amounts.

During SEMAPHORE, the dispersion on $\overline{\phi_p}$ stays below 5% in the mixed layer. A strong synoptic inversion is observed around 2 km on the RH profile. Below the synoptic inversion and above the mixed layer, the large dispersion on the RH profile is caused by the variability of the humidity field associated with the presence of stratocumulus clouds. The large dispersion observed on $\overline{\phi_p}$ around 2 km relates to the fact that the height of the synoptic inversion was different for the six profile average (it ranged from 1.5 to 2 km). Above the synoptic inversion, the troposphere is very dry (Figure 8b). However, because sea-salt and cloud-processed sulfate concentrations diminish with height, $\overline{\phi_p}$ decreases to an average value of 0.0275 sr⁻¹ at 4 km. At this height, RH is equal to 15%. The $\overline{\phi_p}$ related to nucleation sulfate only would be equal to 0.0225 sr⁻¹. The difference between these values means that $\overline{\phi_p}$ is still affected by the presence of sea-salt particles at that height, as a result of the modeled vertical aerosol distribution.

Neglecting the impact of the cloud processing leads to relative errors of 20% and 15% for SOFIA and SEMAPHORE, respectively, on $\overline{\phi_p}$, below 2 km. The corresponding biases are 0.007 and 0.009 sr⁻¹. These errors will have a dramatic impact on the extinction profiles retrieved from lidar measurements, especially above the mixed layer as is shown in section 4.1.

3.2. Near Aircraft Boundary Condition in the Forward Inversion Procedure

The reference backscatter coefficient is obtained from in situ extinction measurements around 0.5 μm made by a nephelometer also installed on the French Atmospheric Research and Teledetection Aircraft. The isokinetic vein configuration is then used to feed aerosols into the nephelometer as in the case of SOFIA. During SEMAPHORE, some of the flights were performed in a configuration without nose boom to enable longer duration flights. The air inlet of the aerosol sampler was fixed on the aircraft itself but was not attached to the isokinetic vein connecting to the nephelometer. Large aerosols were lost, and only the smallest aerosols were detected. As a result, the extinction coefficients could not be measured accurately with the nephelometer in the MABL. However, the extinction measurements in the free troposphere are thought to be reliable since only light particles are generally found away from the continent and in the event that no desert aerosols are advected.

4. Lidar-Derived Extinction Coefficient Profiles

A forward integration scheme [Klett, 1985], which relies on the knowledge of the normalized backscatter phase function $\overline{\phi_p}$ and a value of the aerosol extinction coefficient near the aircraft is applied to the measurements acquired with the airborne backscatter lidar LEANDRE 1. It enables backscatter coefficient profile retrieval throughout the lower troposphere.

Backscatter coefficient profiles result from an accumulation of 12 laser shots, averaged before the inversion procedure is applied. The molecular backscatter coef-

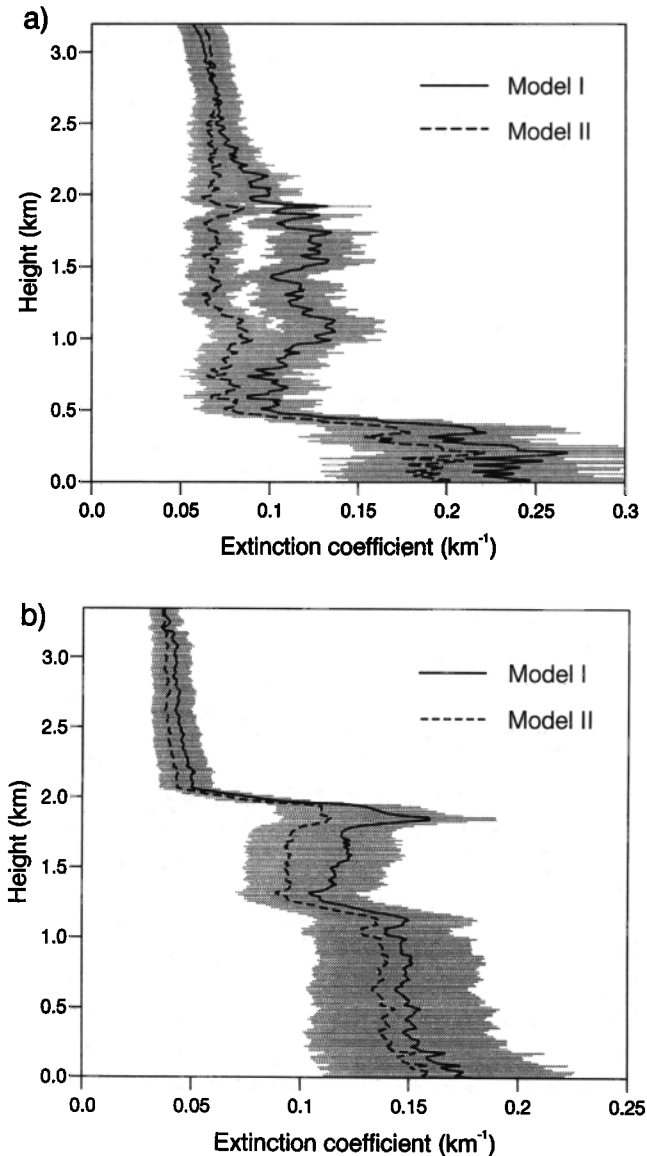


Figure 9. Profile of the extinction coefficient during (a) flight 27 of SOFIA and (b) flight 34 of SEMAPHORE. The solid (dashed) line represents the extinction coefficient profile recovered with a forward lidar inversion procedure using model I (model II). The boundary condition is given by extinction measurements, at the aircraft level, provided by a nephelometer. Error bars result from the sum of all quadratic errors shown in Figure 11.

efficient β_m contribution to the lidar signal is calculated from average pressure and temperature soundings. The reference backscatter coefficient is obtained from in situ extinction measurements around $0.5 \mu\text{m}$ by the nephelometer on board the aircraft. Extinction coefficient profiles are then obtained by dividing the backscatter coefficient profile by the normalized backscatter phase function profile calculated for each flight.

Figure 9a shows an extinction profile, obtained during flight 27 of SOFIA. The normalized backscatter phase function is calculated using the RH profile acquired during flight 27 and the ship measurements of the ASWS.

Average extinction values in the mixed layer (0–0.5 km) and in the subcloud layer (0.5–2.0 km) are equal to 0.21 ± 0.025 and $0.09 \pm 0.02 \text{ km}^{-1}$, respectively. Neglecting the impact of cloudiness and related sulfate processing leads to biases of 0.05 and 0.04 km^{-1} in the mixed layer and above, respectively. The bias on the extinction profile, obtained during flight 34 of SEMAPHORE is smaller. In the mixed layer (0–1.1 km) it is of the order of 0.01 km^{-1} , while above (1.1–2 km) it is equal to 0.02 km^{-1} . The error bars account for uncertainties on the ASWS, RH, and reference extinction. They are discussed in further detail in section 4.1.

Given the errors and biases associated with the inversion procedure, one may wonder whether the inversion is of interest. In order to answer that question we then have compared extinction coefficient profiles recovered while neglecting atmospheric transmission. In this case, the extinction is strictly proportional to the lidar signal and can be obtained by normalizing this signal to the value of the extinction measured on board the aircraft. The "normalized" extinction profiles are compared with the extinction profiles recovered from the inversion using model II (Figure 10). We show a case (flight 27 of SOFIA) where the bias is close to zero between the top of the mixed layer and the synoptic inversion. Above the synoptic inversion, it is of the order of 0.01 km^{-1} . The bias reaches its higher value near the surface where it is equal to 0.015 km^{-1} . On the other hand, in the case of flight 34, the bias can be as large as 0.04 km^{-1} near the surface while being almost zero above the mixed layer. Neglecting the effects of transmission in the mixed layer leads, in this case, to biases larger than the one introduced by the aerosol model. The large bias observed near the surface for flight 34 (Figure 10b) results from the large value of the optical depth in the mixed layer (0.085 and 0.153 for flights 27 and 34, respectively).

At best, the normalization procedure does not introduce any additional bias. Furthermore, the uncertainty in the extinction reference (discussed in section 4.1) will also introduce an error (at least 10%) on the extinction profiles recovered with the normalization procedure.

4.1. Errors on the Extinction Coefficient Profile

The error in the extinction profile retrieved from lidar measurements is related to the uncertainty in the value of BC and in the aerosol normalized backscatter phase function profile. The latter depends on the errors in the measurements of parameters such as relative humidity and ASWS, as well as on the choice of the marine aerosol model (sulfate and sea-salt concentrations, in our case, as well as their vertical distribution). Errors related to signal detection are discarded because the signal-to-noise-ratio is greater than 20 in our case.

The uncertainty in the phase function introduces an error in the extinction coefficient that will propagate away from the source as it affects the transmission cal-

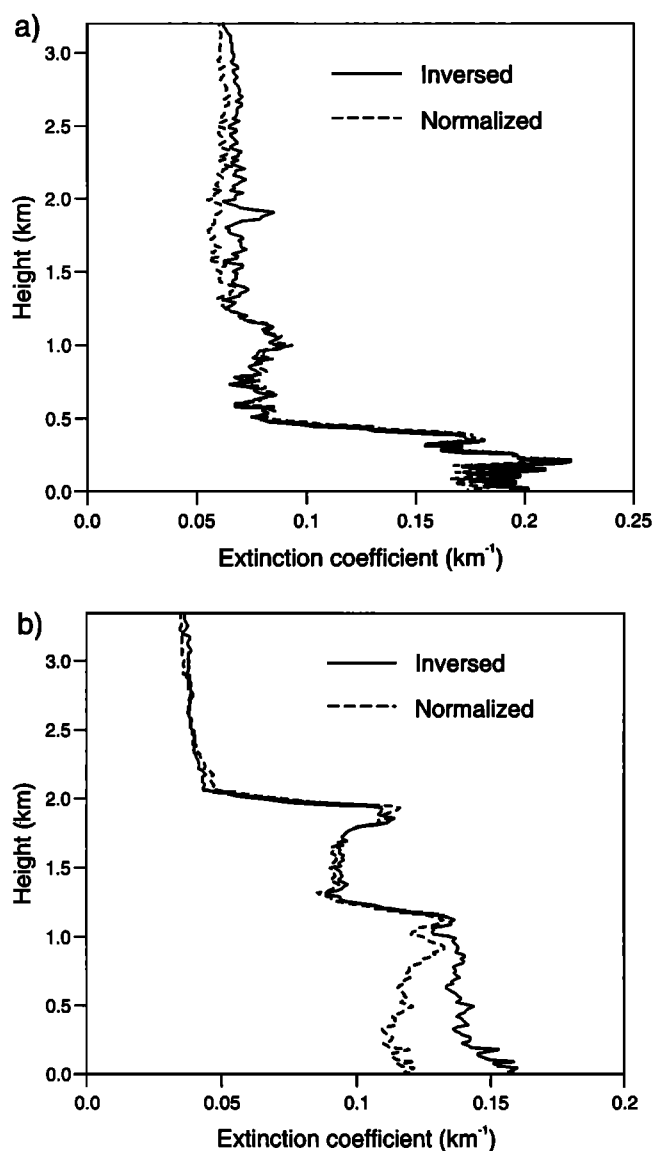


Figure 10. Profile of the extinction coefficient during flight 27 of (a) SOFIA and (b) flight 34 of SEMAPHORE. The solid line represents the extinction coefficient profile recovered with a forward lidar equation inversion procedure using model I. The dashed line represents the extinction coefficient profile obtained when neglecting transmission and normalizing the lidar signal to the value of the extinction measured on board the aircraft.

ulation [Klett, 1981, 1985; Kovalev, 1995]. This error can be discussed from the observed dependence of the phase function on RH and sea-salt fraction (Figure 5). This error can also be calculated analytically [Chazette *et al.*, 1995].

The other source of error stems from the accuracy of the reference backscatter coefficient value used in the inversion procedure. In a forward inversion scheme, the sensitivity to errors in the reference value is increasing away from the reference altitude [Klett, 1981]. This is due to the fact that in the equation used to retrieve the backscatter or the extinction coefficient from lidar

measurements the denominator decreases as the optical thickness increases (see Appendix A). This error can be calculated analytically (see Appendix B).

For an estimated accuracy of 10% in the extinction coefficient measured at the reference altitude, the relative error in the extinction increases to about 20% near the surface (Figure 11). The relative errors related to the uncertainty in the ASWS and RH measurements are small. Since these errors are quadratic, the largest contribution in the free troposphere will originate from the error in the extinction measurements made by the nephelometer.

Accounting for both error sources and accuracy in the measured parameters, the total error in the retrieved extinction coefficients near the surface is thus estimated to be close to 25% for model I and less for model II.

4.2. Extinction Coefficient in the Surface Layer

Initially, in order to assess the reliability of the forward inversion procedure, we intended to compare the extinction coefficient profiles retrieved from lidar measurements with those measured in situ with a nephelometer in the MABL during aircraft soundings. This could have been done for SOFIA only (see section 3.2). However, the air sampled by the instrument is heated before extinction measurements are made, therefore significantly modifying the extinction properties of the aerosol. Above 60% RH, we believe that the nephelometer cannot be reliably used to measure extinction in the MABL. This is why we only used extinction measurements made by this instrument in the free troposphere, even in the case of SOFIA.

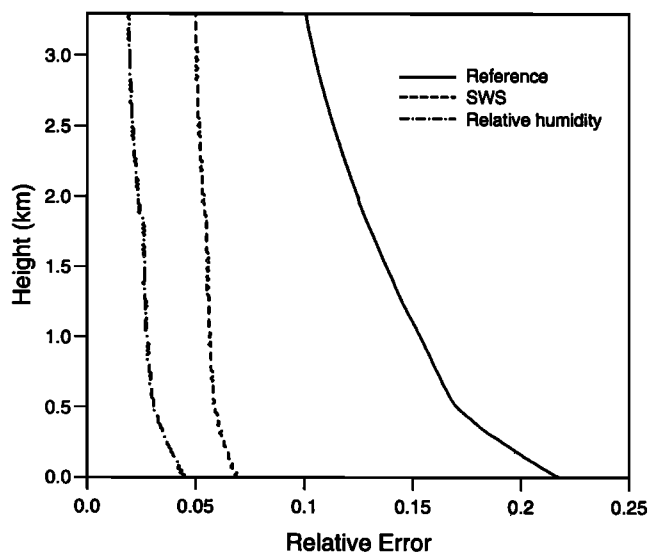


Figure 11. Relative error in the extinction coefficient associated with the uncertainty on the reference extinction value (solid line), the surface wind speed (dashed line), and the relative humidity (dash-dotted line) for model I. Results are shown for a 12-shot average lidar derived extinction coefficient acquired during flight 27 of SOFIA.

Table 3. Correction Factor Used to Normalize Extinction Coefficient to a Reference Relative Humidity Value of 60%

Relative humidity, %	$\alpha / \alpha (60\%)$
65	1.06
70	1.15
75	1.29
80	1.40
85	1.49
90	1.98
95	3.44

We thus needed to compare our results to previously established extinction coefficient dependence on ASWS in order to validate our analysis procedure and determine the sensitivity of the lidar-derived extinctions to the input parameters of the model.

As seen in Table 2, lidar observations were made for RH values in the MABL ranging between 55% and 86%. According to Mie theory, the extinction coefficient would increase, on average, by a factor of about 1.5 between these two RH values (see Table 3). Extinction coefficient ratios shown in Table 3 depend weakly on ASWS.

Lidar-derived extinction coefficients averaged over the first 45 m above the surface and normalized with respect to a reference RH value of 60% are plotted in Figure 12 as a function of 12 hour-averaged SWS. Error bars ($\pm 25\%$) in Figure 12 account for the uncertainty in the reference extinction, ASWS, and RH measurements as discussed in section 4.1. A fair agreement is found between lidar-derived and Mie-computed extinction coefficients with models I and II. A linear fit to the lidar derived extinction coefficient was then performed. On the basis of this fit, extinction between ASWS values of 4 and 10 ms^{-1} is calculated to increase by a factor of 2.0 and 2.3 for models I and II, respectively. However, this increase is not due to an increase of the model-derived normalized backscatter phase function with ASWS in the surface layer (local effect) as shown in Table 2. The values of $\bar{\phi}$ are relatively constant throughout both campaigns. It also is not caused by an increase in the reference extinction used in the inversion procedure. Rather, since the lidar signal in the surface layer is directly proportional to the number concentration in aerosol, the lidar-derived extinction (or backscatter) coefficient should be a linear function of ASWS (see (1)).

However, for an atmosphere characterized by a relatively large optical thickness (more than 0.2), the extinction undergone by the laser beam along the path can be corrected if the normalized backscatter phase function profile is known precisely. Otherwise, the inversion procedure propagates an error away from the altitude of reference as it accounts for the integral of the extinction (see Appendix A). The vertical distribu-

tion of aerosol and RH above the mixed layer can have a dramatic impact on lidar-derived extinction coefficients in the surface layer, as illustrated in Figure 9, where the model induces a relative bias of 20% in the extinction in the case of SOFIA flight 27. The impact of the vertical aerosol and RH distribution (integrated effect) also re-

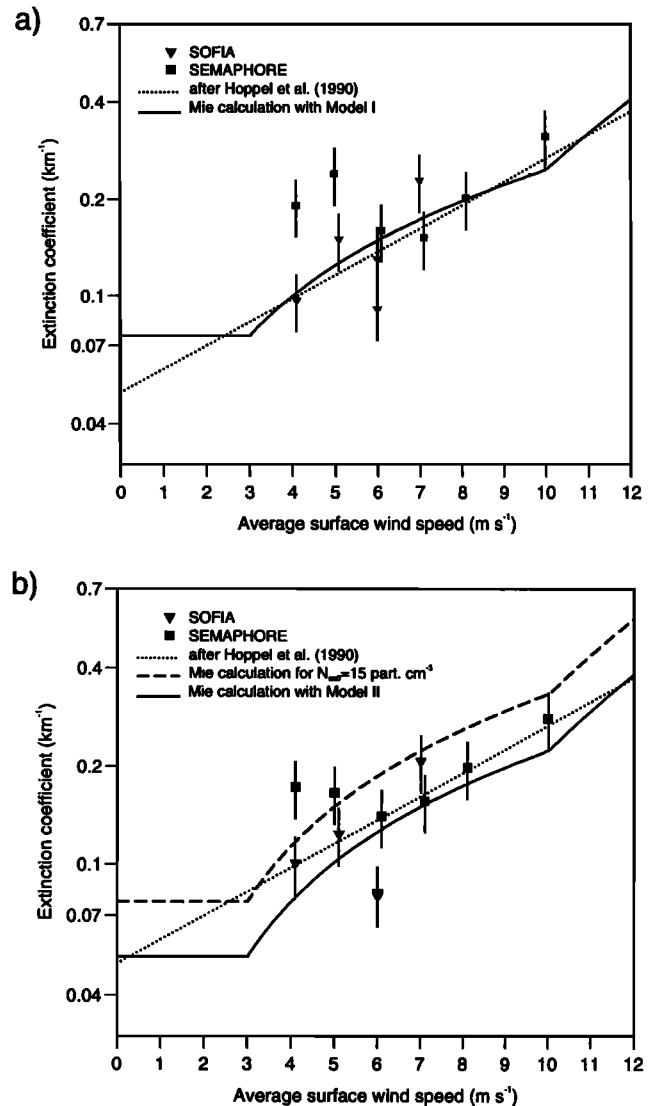


Figure 12. Lidar-derived, near-surface extinction coefficient (squares and triangles), normalized to a relative humidity (RH) of 60%, as a function of the surface wind speed averaged over a 12-hour period prior to the aircraft measurements for (a) model I and (b) model II. In Figure 12(a), the solid line is the extinction coefficient predicted by Mie theory and the dotted line represents the fit to Hoppel et al.'s [1990] extinction measurements given by (8), arbitrarily multiplied by a factor of 2.6. In Figure 12(b), the solid line is the extinction coefficient predicted by Mie theory; the dotted line represents the fit to Hoppel et al.'s [1990] extinction measurements given by (8), arbitrarily multiplied by a factor of 2.6; and the dashed line is the extinction coefficient predicted by Mie theory for N_{se0} equal to 15 particles cm^{-3} (rather than 10 particles cm^{-3} used in models I and II).

Table 4. Impact of the Value of N_{se0} on the Surface Layer Extinction Coefficient (Sea Surface Reflectance)

Flight Number	Extinction, km^{-1}		σ_α , km^{-1}	σ_ρ
	Model I	Model II		
<i>SOFIA</i>				
05	0.138 (0.149)	0.081 (0.145)	0.035	0.030
09	0.144 (0.341)	0.124 (0.277)	0.036	0.077
11	0.091 (0.313)	0.082 (0.295)	0.023	0.075
13	0.095 (0.318)	0.101 (0.345)	0.024	0.103
27	0.229 (0.294)	0.188 (0.282)	0.057	0.058
<i>SEMAPHORE</i>				
30	0.160 (0.502)	0.141 (0.478)	0.040	0.177
31	0.191 (0.208)	0.173 (0.218)	0.047	0.060
32	0.314 (0.143)	0.282 (0.127)	0.078	0.029
33	0.240 (0.142)	0.166 (0.124)	0.060	0.028
34	0.152 (0.101)	0.157 (0.115)	0.038	0.025
35	0.202 (0.094)	0.199 (0.089)	0.050	0.024
Average	0.177 (0.237)	0.156 (0.227)	0.044	0.062

Numbers in parentheses denote reflectance values. Here σ_α (σ_ρ) is the 25% error associated with the inversion procedure for model I on the extinction coefficient (reflectance) in the surface layer.

sults in a greater scatter of the lidar-derived extinctions when using model I. The standard deviation around the fitted linear regression is equal to 0.052 and 0.042 km^{-1} for models I and II, respectively. Some of the dispersion observed in Figures 12a and 12b is also likely related to uncertainties in the ASWS measurements (probably larger than the 1 ms^{-1} systematic error accounted for in this study) and in the cloud cover (and the sulfate related extinction) which are not known.

In Table 4, we illustrate the impact of the aerosol model on the retrieval of the surface layer extinction coefficient. The average bias (or difference between the extinction coefficients retrieved with models I and II, $\Delta\alpha = |\bar{\alpha}_I - \bar{\alpha}_{II}|$), is smaller than the 25% error associated with the inversion procedure for model I ($\sigma_\alpha = 0.3\bar{\alpha}_I$) (0.02 versus 0.044 km^{-1}). However, the bias can be much larger for a given flight (see the discussion for SOFIA flight 27 in section 4.1).

Finally, we studied the sensitivity of the extinction retrievals to the vertical distribution of stationary marine aerosols in the model (namely, the value of H in(2)). Jaenicke [1993] reports a great diversity of values for H (between 0.5 and 2 km). The average difference between the extinction coefficients retrieved with model I for $H=2$ km and $H=0.5$ km is also smaller than the 25% error associated with the inversion procedure (0.01 versus 0.044 km^{-1}).

We now study the extinction dependence on ASWS. A relationship between in situ extinction measurements at 0.55 μm and ASWS has been proposed by Hoppel et al. [1990], over the Atlantic Ocean, in the form of

$$\alpha = 0.025 \exp(0.1689\bar{U}). \quad (8)$$

Hoppel et al.'s [1990] data were obtained in prevailing open ocean conditions: 12 out of 16 days were characterized by Radon concentrations of 2-3 pCi m^{-3} , typical for the marine background level over the Atlantic. Four days were characterized by Radon concentrations between 3 and 10 pCi m^{-3} , indicative of polluted air masses originating from the United States. Given the total aerosol content typical of open ocean conditions and the reference relative humidity (75%) reported by Hoppel et al. [1990], we had to arbitrarily divide our modeled extinction coefficients by a factor of 2.6 in order to match extinctions obtained with (8). This discrepancy is likely related to the value of N_{se0} to be used in order for our extinction measurements to fit Hoppel et al.'s. It could be caused by the variability of the background marine sea-salt distribution, which is a function of time and location, as discussed by Gong et al. (1997). For example, with a value of $N_{se0}=4$ particles cm^{-3} , our extinction measurements would match those of Hoppel et al. [1990].

Nevertheless, the general trend of our lidar-derived extinction coefficients is correctly predicted by (8). Our best exponential fit to the data yields

$$\begin{cases} \alpha_I = 0.079 \exp(0.1199\bar{U}), \\ \alpha_{II} = 0.063 \exp(0.1302\bar{U}), \end{cases} \quad (9)$$

where subscripts I and II refer to models I and II, respectively.

The correlation coefficients between our lidar-derived extinction and Hoppel et al.'s [1990] fit are equal to 0.65 and 0.75 for models I and II, respectively. The lidar-derived extinction deviations from Hoppel et al.'s

[1990] fit are 0.0049 and 0.0038 km⁻¹ for models I and II, respectively.

5. Sea Surface Reflectance

In this section, the relationship between ocean surface reflectance and backscatter coefficient above the ocean surface is used to examine the dependence of the retrieved surface wind speed on the aerosol model. As illustrated by Figure 10b, in cases where the optical depth is larger than 0.2, the bias in the extinction in the surface layer introduced while neglecting the effect of transmission is greater than the bias related to the choice of the aerosol model. Previous studies on laser backscatter dependence on wind speed [Bufton *et al.*, 1983] were conducted in the MABL. Bufton *et al.* [1983] did not attempt to correct for transmission effects. It is the purpose of this section to show that the inversion of lidar measurements is highly desirable when studying sea surface reflectance properties.

From the estimate of the backscatter coefficient in the first tens of meters above the surface, obtained with and without the forward inversion, we determine sea surface reflectance. We then compare these values with those retrieved independently from the measured wind speed using a sea surface reflectance model.

5.1. Lidar-Derived Sea Surface Reflectance

In Appendix C, we derive the relationship between the equivalent directional ocean surface reflectance $\hat{\rho}$ observed by lidar and the average backscatter coefficient measured in a layer of depth Δz , at an altitude $z_b = z_0 + \Delta z$ above the surface. This relationship accounts for the lidar signal $S(\lambda, z_b)$ in the layer close to the surface, and for the lidar surface return signal $S(\lambda, z_0)$. It is written as [Chazette, 1990]

$$\hat{\rho} = \pi \Delta z \beta(\lambda, \pi, z_b) \frac{S(\lambda, z_0)}{S(\lambda, z_b)}. \quad (10)$$

It should be noted that this relationship can also be reversed to derive the atmospheric backscatter coefficient near the surface, whenever direct directional ocean surface reflectance measurements are available [Reagan and Zielinski, 1991]. In the present analysis, since we have selected the forward inversion scheme, both extinction coefficients in the ABL and SWS can be retrieved from surface reflectance modeling.

5.2. Sea Surface Reflectance Modeling

Light reflection by the ocean surface has been observed to be dependent on the small wave facets that are produced by capillary and gravity waves at the surface [Cox and Munk, 1954; Bufton *et al.*, 1983]. The angular spread of these facets is defined by the distribution of wave slopes. As the optical wavelength of light is much

smaller than the capillary waves, laws relevant to geometric optics can be used in the analysis. In this case the mean-square wave slope $\langle S^2 \rangle$ is the parameter that controls the reflectance variation with wind speed. In an earlier work by Cox and Munk [1954], the mean square wave slope statistics have been observed to follow a near-Gaussian distribution in a two-dimensional plane, when wind direction effects are not considered. The mean square wave slope was found to depend on the instantaneous surface wind speed (ISWS), denoted U (observed over a period of a few minutes, as opposed to the time averaged wind used in the aerosol model), measured at 12 m, according to

$$\langle S^2 \rangle = \langle S_u^2 \rangle + \langle S_v^2 \rangle, \quad (11)$$

$$\langle S^2 \rangle = 0.003 + 5.12 \cdot 10^{-3} U, \quad (12)$$

where u and v are the along- and cross-wind components. In the case of lidar measurements (same off-nadir angle γ in incidence and reflection with respect to the vertical), the sea surface reflectance is given by Cox and Munk [1954]

$$\rho_s = \frac{\rho_o}{4 \langle S^2 \rangle \cos^6 \gamma} \exp\left(-\frac{\tan^2 \gamma}{\langle S^2 \rangle}\right), \quad (13)$$

where ρ_o is the reflectance given by Fresnel equations at the air-sea interface ($\rho_o = 0.0204$ at 0.532 μm). In this expression, the effects of laser pulse shape and divergence have been neglected as contributing very weakly owing to our measurement configuration [Gardner *et al.*, 1983]. The light backscattered from the first meters below the ocean surface also contributes to the measured surface reflectance as $\hat{\rho} = \rho_s + \rho_{ssw}$. The volumic reflectance ρ_{ssw} of the subsurface water has been reported to be smaller than 0.02 over a large set of open ocean waters [Morel and Prieur, 1977]. This term is thus much smaller than ρ_s at low wind speed and is neglected in this first approach. Furthermore, foam is not expected to contribute significantly to the reflectance, as observations are reported for wind speeds below 10 ms⁻¹. Sun radiance is also treated as negligible noise.

Backscattering vertical profiles retrieved from lidar measurements using aerosol model I have been used in the ISWS analysis. Sea surface reflectance values are derived using (10) (section 5.1) from near-surface backscatter. The ISWS used in this model is taken closest in time to the lidar measurements. Figure 13 stresses the variability of reflectance over a distance of 4 km, as measured during flight 30 of SEMAPHORE. Values of the reflectance were inferred from 24 averaged lidar shots (it corresponds to a time average of 2 s or about 170 m in distance), in order to reduce the uncertainty introduced by a low signal-to-noise ratio. Error bars on reflectance are derived from error con-

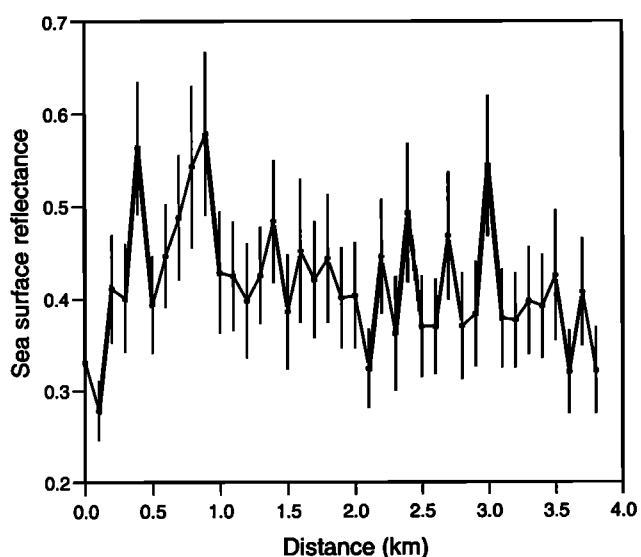


Figure 13. Horizontal fluctuations of the ocean surface reflectance, derived from lidar measurements using (10), during flight 30 of SEMAPHORE.

siderations in the extinction discussed in section 4. A large variability is observed, which, at times, may be greater than the uncertainty associated with the forward inversion procedure. It is also observed that the relative standard deviation of the reflectance is about 0.1. This value is larger than the one obtained by using Jackson's equation as reported by *Bufton et al.* [1983]. This could result from the noise introduced in the inversion procedure, as discussed before, or from large waves enhancing specular reflection at the sea surface. Since the footprint of the laser is about 15 m in diameter and the total area covered while averaging 24 profiles is $15 \times 170 \text{ m}^2$, the wave reflection enhancement may induce correlation between shots, which may be minimized in case of a cross-wave observation. This point will be further investigated in future campaigns, taking into account the impact of wind and swell direction.

The average sea surface lidar-derived reflectance values are plotted in Figure 14 as a function of the ISWS and compared with Cox and Munk's [1954] model. Error bars include the error stemming from our analysis procedure and the estimated variability from the individually measured reflectances along the flight track (Figure 13). A good agreement is observed between our results and the two-dimensional model of Cox and Munk [1954]. As seen from (10), the reflectance retrieved from measurements is sensitive to the backscatter coefficient, which is the product of the extinction coefficient and the phase function. Referring to the previous analysis, one notices that extinction is decreased when using aerosol model I, instead of model II. This is the reverse of the phase function. The backscatter and the deduced reflectance are thus weakly dependent on the aerosol model hypothesis. In fact, it is found

that the standard deviation between reflectance values derived using both aerosol models is about 10%. Furthermore, the value of N_{se0} does not have a significant impact on surface wind retrievals. As uncertainties in the observation angle may exist in the case of airborne measurements, the reflectance was also modeled for a

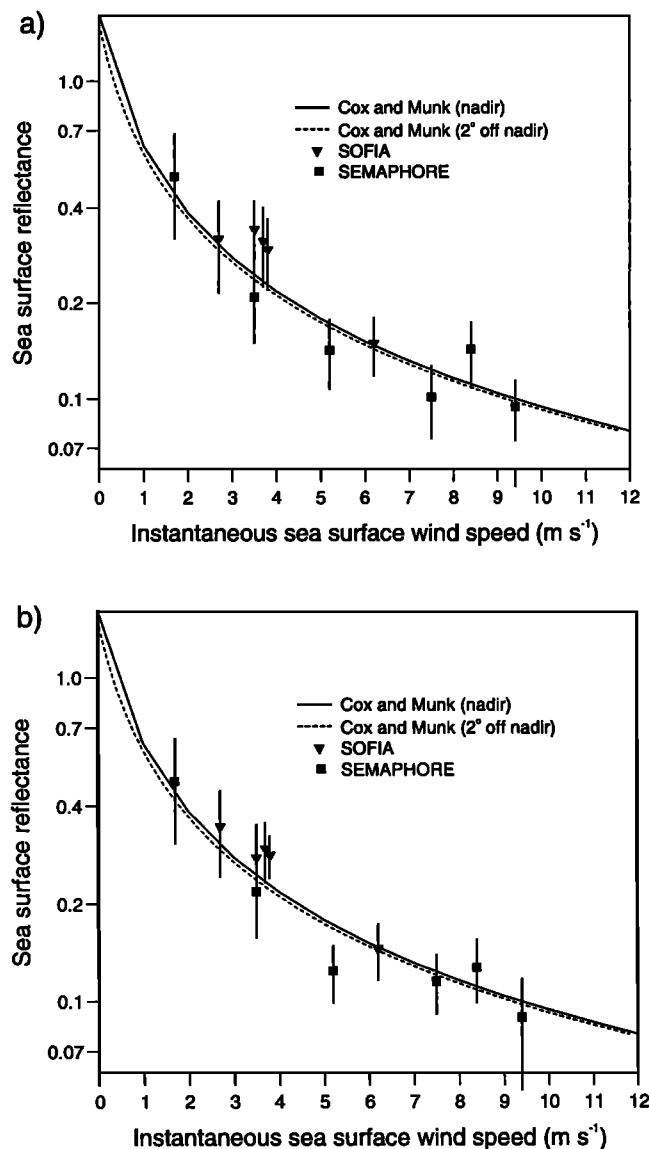


Figure 14. Sea surface reflectance retrieved from lidar as a function of the surface wind speed for (a) model I and (b) model II. The error bars are related to the uncertainty on the normalized backscatter phase function and signal fluctuations. The reflectance calculated using Cox and Munk's [1954] model for an incidence angle of zero (corresponding to nadir lidar measurements) and 2° (corresponding to off-nadir lidar measurements, respectively) is given by the solid and dashed lines, respectively. Here ΔU is the difference between the measured instantaneous surface wind speed (ISWS) and the ISWS inferred from Cox and Munk's [1954] reflectance model using the lidar-derived extinction coefficients obtained with a forward inversion procedure.

Table 5. Flight Average Values of Instantaneous Surface Wind Speed (ISWS) and Differences ΔU Between Measured ISWS and ISWS Inferred from Cox and Munk's [1954] Reflectance Model Using Lidar-Derived Extinction Coefficients Obtained with a Forward Inversion Procedure and Without Inversion.

Flight Number	ISWS, m s^{-1}	ΔU , m s^{-1}		
		Model I	Model II	No Inversion
<i>SOFIA</i>				
05	6.2	0.1	0.0	-0.4
09	3.5	1.2	0.5	0.0
11	3.7	1.1	0.9	0.5
13	2.7	0.2	0.4	0.0
27	2.8	1.0	0.9	-1.5
<i>SEMAPHORE</i>				
30	1.7	0.3	0.2	0.3
31	3.5	-0.7	-0.5	-1.2
32	8.4	2.0	1.1	3.3
33	5.2	-1.2	-2.2	-4.4
34	7.5	-1.8	-0.5	-1.7
35	9.4	-0.6	-1.2	-2.5

2° angle off nadir. Pitch-, roll-, and yaw-related uncertainties, which are much smaller than 2° , are not an important source of error as shown by Figure 14.

Inversely, one can estimate the ISWS from lidar measurements, using the Cox and Munk [1954] model. Intraflight differences ΔU_i between the measured ISWS and the ISWS derived from the retrieved reflectance (using (12) and (13)) are given in Table 5 for the two aerosol models. For model I, the residual bias on the ISWS (calculated as $\sum_{i=1}^N \Delta U_i / N$) is 0.11 m s^{-1} and the standard deviation is about 1.2 m s^{-1} . For model II, the residual bias on the ISWS is -0.04 m s^{-1} and the standard deviation is 0.9 m s^{-1} . The standard deviation associated with these retrievals is of the order of the uncertainty on the measurements themselves. This confirms that the wind speed estimation below 10 m s^{-1} is not very sensitive to the aerosol model used in the inversion procedure. However, as stressed in section 4, it is necessary to use an inversion procedure in order to retrieve the extinction coefficient in the surface layer from lidar measurements and infer wind speed from these measurements! To further emphasize this necessity, we performed the same calculation using the values of the surface layer extinctions recovered with the normalization procedure rather than the inversion procedure. The residual bias on the ISWS is then -0.7 m s^{-1} , and the standard deviation is 1.95 m s^{-1} . Both the bias and standard deviation are significantly larger when using the former rather than the latter procedure.

The next step was to assess the reliability of the inferred ISWS with the technique described above for low wind speed and high wind speed regimes. We have separated the data using a value of 4 m s^{-1} as a threshold. This value was dictated by the fact that we want the

statistics of both groups to be representative given the small number of data. Five flights were characterized with ISWS values above 4 m s^{-1} , and six had ISWS values below 4 m s^{-1} . For the low ISWS regime, the biases (0.5 , 0.4 , and -0.3 m s^{-1} for the inversion procedure model I, model II, and the normalization procedure, respectively) and standard deviations (0.7 , 0.5 , and 0.8 m s^{-1}) are in good agreement. For the high ISWS regime, however, the biases (-0.3 and -0.5 m s^{-1} , for models I and II, respectively) and standard deviations (1.5 and 1.3 m s^{-1}) are significantly smaller than the bias (-1.2 m s^{-1}) and standard deviation (2.9 m s^{-1}) retrieved using the normalization procedure. This result stems from the fact that larger wind speeds generate a greater amount of particles to which the lidar signal is sensitive. The greater the number of particles is, the larger the optical depth is and the greater the necessity is to use an inversion procedure to determine the extinction coefficient near the surface.

6. Summary and Conclusion

A marine aerosol model, based on measured distribution parameterization and including the effects of humidity, is used to analyze lidar data from flights performed over the Azores during the SEMAPHORE and SOFIA/ASTEX experiments. Precision in the modeled normalized aerosol backscatter phase function is of the order of 5% for a given model. However, the uncertainty associated with cloud processing can be as high as 20%. In the absence of desert or volcano dust, in the relatively clear air characterizing the open ocean air masses, the modeled normalized aerosol backscatter phase function is used in a forward lidar equation inver-

sion procedure in order to retrieve accurate backscatter coefficient profiles in the MABL. Surface layer extinction at $0.532 \mu\text{m}$ is obtained with a 25% accuracy and depends on the surface wind speed as previously observed. Provided that the surface return in the lidar signal is not saturated, we establish a relationship between ocean reflectance and the backscatter coefficient above the surface. Sea surface reflectance values, determined from lidar-derived backscatter coefficients and the previously established reflectance-backscatter relationship, are found in excellent agreement with those predicted, as a function of wind speed, by the reflectance model of *Cox and Munk* [1954]. The sensitivity of the inversion procedure to the aerosol model (presence or absence of an accumulation mode for sulfate, vertical distribution of stationary marine components above the MABL) has also been tested on the surface layer extinction coefficient and sea surface reflectance. Differences in extinction values between models remained smaller than the 25% error associated with the forward inversion procedure in the surface layer. This implies that, for now, the choice of the model is not crucial. However, as stressed in sections 4 and 5 it is necessary to use an inversion procedure in order to retrieve the extinction coefficient in the surface layer from lidar measurements and, in turn, infer wind speed, especially for surface wind speeds larger than 4 ms^{-1} . Moreover, in the event that the uncertainty in the reference extinction and in the sulfate concentration (the two largest sources of error in our case) can be reduced, the choice of the model will be important. The major concerns for the analysis of measurements made by a remote sensing instrument operating in the visible, is the particle size distribution and composition of the accumulation mode. Comparison with the extinction measurements of *Hoppel et al.* [1990] (at a wavelength close to that of the lidar) suggest a significant difference in background sea-salt concentration over the different parts of the northern Atlantic Ocean that may be related to the action of wind on the surface.

Given the large variety of particle concentrations reported in the literature, lidar measurements have proven to be valuable with respect to choosing the number of sea-salt and sulfate aerosols. Not just any value will enable the lidar-derived and Mie-calculated extinction coefficients to converge within a few tens of percents in the surface layer (where the error is greatest). In the absence of sulfate processing by clouds, the lidar-derived reflectance seem in better agreement with the model of *Cox and Munk* [1954]. However, this would mean that the air masses did not experience cloudy conditions on any of the 11 cases studied, which is highly improbable. Rather, we believe that since CPE depends on the cloud cover, the value of $65 \text{ particles cm}^{-3}$ is not necessarily representative of the production by clouds along each air mass trajectory. Further studies should address this important issue.

The validation of the reflectance-backscatter relationship in open ocean conditions is an important step toward the use of lidar measurements for ABL analysis. It is also a first step toward a global analysis using future spaceborne lidar data, as planned by space agencies. This relationship provides an attractive boundary condition for backward lidar equation inversion procedures, provided that there exist measurements of the wind speed in the surface layer. In the case of a relatively clear atmosphere (small optical thickness), another interesting prospect concerns the use of this relationship for surface wind speed retrievals. Future studies should address the possibility of determining the aerosol normalized backscatter phase function iteratively, assuming no a priori knowledge of the surface wind speed. Whenever the fractional area covered by whitecaps is small, as is the case in low wind speed regimes, lidars could be used complementary to scatterometers to provide surface wind speed estimates. This approach will be tested in the framework of the Flux, États de mer et Télédétection en Conditions de Fetch variable (FETCH) experiment (spring 1998) over the Mediterranean.

Appendix A: Derivation of the Backscatter Coefficient from Lidar Measurements

The optical power backscattered to the telescope by molecules and particles in an atmospheric layer located at an altitude z is given by *Measures* [1984]

$$P(\lambda, z) = \frac{C(\lambda)}{(z_a - z)^2} \beta(\lambda, \pi, z) T^2(\lambda, z, z_a), \quad (\text{A1})$$

with

$$C(\lambda) = \frac{c}{2} \mu^2 E_0(\lambda) \eta(\lambda) A, \quad (\text{A2})$$

where c is the light velocity; η accounts for the detection chain quantum efficiency and optical throughput; A is the collecting area of the telescope; $\mu = \cos(\gamma)$, where γ is the reflection angle; E_0 is the laser output energy; z_a is the altitude of the laser source; and $T(\lambda, z, z_a)$ is the atmospheric transmittance from z to z_a given by

$$T^2(\lambda, z, z_a) = \exp \left[-2 \int_z^{z_a} \alpha(\lambda, z') dz' \right]. \quad (\text{A3})$$

Our aim is to retrieve β and α in the lower troposphere. We define a linear relationship between backscatter and extinction coefficients for molecules and particles as

$$\beta_i(\lambda, \pi, z) = \phi_i(\lambda, z) \alpha_i(\lambda, \pi, z), \quad (\text{A4})$$

where i stands for either molecules (m) or particles (p). Equation (A1) can now be solved for β or α indifferently. For a monostatic, monochromatic, pulsed lidar, the expression of the backscatter coefficient is obtained by solving a Bernoulli type differential equation [*Klett*, 1981, 1985]. The unstable solution is given by

$$\beta(\lambda, \pi, z) = \frac{(z_a - z)^2 P(\lambda, z) Q(\lambda, z)}{\frac{(z_a - z_r)^2 P(\lambda, z_r)}{\beta(\lambda, \pi, z_r)} - 2 \int_{z_r}^z \frac{(z_a - z')^2 P(\lambda, z') Q(\lambda, z')}{\phi(\lambda, z')} dz'}, \quad (\text{A5})$$

where z_r is the altitude of the boundary condition necessary for the integration and $Q(\lambda, z)$ is given by

$$Q(\lambda, z) = \exp \left[2 \left[\frac{\phi_m}{\phi_p} - 1 \right] \int_{z_r}^z \alpha_m(\lambda, z') dz' \right]. \quad (\text{A6})$$

The procedure described in this appendix is generally referred to as the lidar equation inversion procedure.

Appendix B: Sensitivity of the Lidar Inversion to the Uncertainty on the Boundary Condition and on the Normalized Backscatter phase Function

The backscatter coefficient expressed by (A5) can be written

$$\beta(\lambda, \pi, z) = \frac{N(z)}{D(z)}, \quad (\text{B1})$$

where

$$N(z) = (z_a - z)^2 P(\lambda, z) Q(\lambda, z), \quad (\text{B2})$$

$$D(z) = -2 \int_{z_r}^z \frac{(z_a - z')^2 P(\lambda, z') Q(\lambda, z')}{\phi(\lambda, z')} dz' + \frac{(z_a - z_r)^2 P(\lambda, z_r)}{\beta(\lambda, \pi, z_r)}. \quad (\text{B3})$$

The statistical error in the backscatter coefficient can be estimated as a function of the reference backscatter coefficient and the uncertainty of this reference value [Chazette *et al.*, 1995]. It is supposed that it is independent of any other uncertainty such as the one on the normalized backscatter phase function. The error due to the signal normalization is negligible because of the high signal to noise ratio close to the source. The relative error $\epsilon_\beta(\lambda, z)$ on the backscatter coefficient is defined as

$$\epsilon_\beta(\lambda, z) = \left[\frac{\text{Var} \beta(\lambda, \pi, z)}{\beta^2(\lambda, \pi, z)} \right]^{1/2}, \quad (\text{B4})$$

where $\text{Var}(\beta)$ defines the variance related to the backscatter coefficient.

In forward inversion procedures, the relative error can be expressed as a function of the relative error on the reference extinction value measured by the nephelometer, $\epsilon_n(\lambda, z_r)$, as

$$\epsilon_{\beta-f}(\lambda, z) = \left[\frac{(z_0 - z_r)^2 P^2(\lambda, z_r)}{D^2(z) \beta^2(\lambda, \pi, z_r)} \right]^{1/2} \epsilon_n(\lambda, z_r). \quad (\text{B5})$$

The relative error in the backscatter coefficient related to the relative error on the normalized backscatter phase function is given by Chazette *et al.* [1995].

Appendix C: Determination of the Sea Surface Reflectance from the Lidar Signal Surface Echo

The bidirectional reflectance of the surface ρ considered as Lambertian, is defined by the relation

$$\rho(\lambda, \gamma_i) = \frac{\pi L_i(\lambda)}{\mu_i E_i(\lambda)}, \quad (\text{C1})$$

where L_i is the radiance of a Lambertian surface; E_i is the incident irradiance and $\mu_i = \cos(\gamma_i)$, where γ_i is the angle of incidence and observation. In the case of a monostatic lidar, the solid angle of emission is given by

$$\Omega = \frac{R \mu^3}{(z_a - z_0)^2}, \quad (\text{C2})$$

where R is the area of the footprint of the laser beam on the ocean surface, z_a is the altitude of the aircraft, and z_0 refers to sea level. The power backscattered by the surface is given by

$$P_d(\lambda, z_0) = L_i(\lambda) A \Omega \exp \left[-\frac{\tau(\lambda, z_a, z_0)}{\mu} \right], \quad (\text{C3})$$

where A is the collecting area of the telescope; τ is the one-way attenuation between the aircraft and the surface. Combining (C1), (C2), and (C3), we obtain

$$P_d(\lambda, z_0) = \rho(\lambda, \gamma) \frac{\mu^4}{\pi} E_i(\lambda) \frac{A R}{(z_a - z_0)^2} \exp \left[-\frac{\tau(\lambda, z_a, z_0)}{\mu} \right], \quad (\text{C4})$$

The incident irradiance can be expressed as a function of the emitted laser power P_0 (attenuated one way as it propagates toward the surface) by

$$E_i(\lambda) = \frac{P_0(\lambda)}{R} \exp \left[-\frac{\tau(\lambda, z_a, z_0)}{\mu} \right]. \quad (\text{C5})$$

We can then write the expression of the power collected by the telescope under the form

$$P_d(\lambda, z_0) = \rho(\lambda, \gamma) \frac{\mu^4}{\pi} P_0(\lambda) \frac{A}{(z_a - z_0)^2} \exp \left[-2 \frac{\tau(\lambda, z_a, z_0)}{\mu} \right]. \quad (\text{C6})$$

For a pulsed lidar (whose pulse duration is small compared to the time of propagation of the beam from the aircraft to the surface) having a vertical resolution of Δz , the instantaneous power P_d received on the detector is given by

$$P_d(\lambda, z_0) = \frac{c}{2} \rho(\lambda, \gamma) \frac{\mu^3}{\pi} E_0(\lambda) \eta(\lambda) \frac{A}{(z_a - z_0)^2 \Delta z} \exp \left[-2 \frac{\tau(\lambda, z_a, z_0)}{\mu} \right], \quad (C7)$$

where c is the light velocity, E_0 is the laser output energy, and η is the overall detection efficiency. Using (A2), the power backscattered to the telescope is rewritten as:

$$P_d(\lambda, z_0) = \rho(\lambda, \gamma) \frac{C(\lambda)}{(z_a - z_0)^2} \frac{\mu}{\pi \Delta z} \exp \left[-2 \frac{\tau(\lambda, z_a, z_0)}{\mu} \right]. \quad (C8)$$

Using (A1) and (A3), we express the equivalent lidar reflectance as a function of the backscatter coefficient and the optical power backscattered from an altitude z_b in the surface layer and by the surface as

$$\rho = \frac{\pi \Delta z}{\mu} \beta(\lambda, \pi, z_b) \frac{P_d(\lambda, z_0)}{P_d(\lambda, z_b)}, \quad (C9)$$

with $\mu=1$ for a nadir pointing lidar system. The ratio $P_d(\lambda, z_0)/P_d(\lambda, z_b)$ can be written as a function of the ratio of lidar signal $S(\lambda, z_0)/S(\lambda, z_b)$.

Acknowledgments. The authors want to thank P. H. Flamant, R. T. Menzies, and F. Dulac for helpful discussions. They are indebted to their colleagues R. Valentin and S. Elouragini for their participation in the flights during the SOFIA and SEMAPHORE experiments. Special thanks go to C. Allet for the processing of in situ aircraft data. This research was funded by CNRS and IFREMER through the Programme Atmosphère Océan à Moyenne Echelle and by the European Space Agency, which are acknowledged. The authors would also like to thank the anonymous reviewers for their helpful comments and suggestions.

References

- Albrecht, B. A., C. S. Bretherton, D. W. Johnson, W. H. Schubert, and A. S. Frisch, The Atlantic Stratocumulus Transition Experiment-ASTEX., *Bull. Am. Meteorol. Soc.*, **76**, 889-904, 1995.
- Blanchard, C. D., and A. H. Woodcock, The production, concentration, and vertical distribution of the sea-salt aerosols, *Ann. N. Y. Acad. of Sci.*, **338**, 330-347, 1980.
- Blanchard, C. D., A. H. Woodcock, and R. J. Cipriano, The vertical distribution of concentration of sea salt in the marine atmosphere near Hawaii, *Tellus, Ser. B*, **36**, 118-125, 1984.
- Boers, R., S. H. Melfi, and S. P. Palm, Cold-air break during GALE: Lidar observation and modelling of boundary layer dynamics, *Mon. Weather Rev.*, **119**, 1132-1150, 1990.
- Buften, J. L., F. E. Hoge, and R. N. Swift, Airborne measurements of laser backscatter from the ocean surface, *Appl. Opt.*, **22**, 2603-2618, 1983.
- Charlson, R. J., S. E. Schwartz, J. M. Hales, R. D. Cess, J. A. Coakley Jr., E. Hansen, and D. J. Hofmann, Climate forcing by anthropogenic aerosols, *Science*, **255**, 423-430, 1992.
- Chazette P., Étude complémentaire des systèmes de télédétection laser et des sondeurs passifs pour la détermination des paramètres météorologiques à partir de plateformes spatiales, PhD thesis, 338 pp., University Pierre et Marie Curie, Paris, May 1990.
- Chazette P., C. David, J. Lefrère, S. Godin, J. Pelon, and G. Mégie, Comparative lidar study of the optical, geometrical, and dynamical properties of stratospheric post-volcanic aerosols, following the eruptions of El Chichon and Mount Pinatubo, *J. Geophys. Res.*, **100**, 23,195-23,207, 1995.
- Cox, C., and W. Munk, Measurements of roughness of the sea surface from photographs of the Sun's glitter, *J. Opt. Soc. Am.*, **44**, 832-850, 1954.
- De Leeuw, G., Modeling of extinction and backscatter profiles in the marine mixed layer, *Appl. Opt.*, **28**, 7, 1989.
- Dupont, E., J. Pelon, and C. Flamant, Study of the moist convective boundary layer structure by backscatter lidar, *Boundary-Layer Meteorol.*, **69**, 1-25, 1994.
- Exton, H. J., J. Latham, P.M Park, S. J. Perry, M. H. Smith, and R. R. Allan, The production and the dispersal of marine aerosol, *Q. J. R. Meteorol. Soc.*, **111**, 817-837, 1985.
- Eymard, L. et al., Study of the air-sea interaction at the mesoscale: The SEMAPHORE Experiment, *Ann. Geophys.*, **14**, 986-1015, 1996.
- Fairall, C. W., K. L. Davidson, and G. E. Schacher, Application of a mixed layer model to aerosols in the marine boundary layer, *Tellus, Ser. B*, **36**, 203-211, 1984.
- Fitzgerald, J. W., W. A. Hoppel, and M. A. Vietti, The size and scattering coefficient of urban particles at Washington DC, as a function of relative humidity, *J. Atmos. Sci.*, **39**, 1838-1852, 1982.
- Flamant, C., and J. Pelon, Atmospheric boundary-layer structure over the Mediterranean during a Tramontane event, *Q. J. R. Meteorol. Soc.*, **122**, 1741-1778, 1996.
- Fouquart, Y., and H. Isaka, Sulfur emissions, CCN, clouds and climate: A review, *Ann. Geophys.*, **10**, 462-471, 1992.
- Gardner, C. S., B. M. Tsai, and K. E. Im, Multicolor laser altimeter for barometric measurements over the ocean: Theoretical, *Appl. Opt.*, **22**, 2571-2577, 1983.
- Gathman, S. G., Optical properties of the marine aerosols as predicted by the Navy aerosol model, *Opt. Eng.*, **22**, 57-62, 1983.
- Gathman, S. G., G. de Leeuw, K. L. Davidson, and D. R. Jensen, The Naval oceanic vertical aerosol model: Progress report, Atmospheric Propagation in the UV, Visible, IR and MM-Wave Region and Related Systems Aspects, Advanced Group for Res. and Dev., Brussel, 1989.
- Gong, S. L., L. A. Barrie, and J.-P. Blanchet, Modeling the sea-salt aerosols in the atmosphere, 1, Model development, *J. Geophys. Res.*, **102**, 3805-3818, 1997.
- Hänel, G., The properties of atmospheric aerosol particles as functions of the relative humidity at thermodynamic equilibrium with the surrounding moist air, *Adv. Geophys.*, **19**, 73-188, 1976.
- Hegg, D. A., P. F. Yuen, and T. V. Larson, Modeling the effects of heterogeneous cloud chemistry on the marine particle size distribution, *J. Geophys. Res.*, **97**, 12,917-12,933, 1992.
- Hegg, D. A., R. J. Ferek, and P. V. Hobbs, Aerosol size distributions in the cloudy atmospheric boundary layer of the North Atlantic Ocean, *J. Geophys. Res.*, **98**, 8841-8846, 1993.
- Heinmann, M., The Global Atmospheric Tracer Model TM2, Rep. 10, Max Planck Inst. für Meteorol., Hamburg, Germany, 1995.
- Hoppel, W. A., J. W. Fitzgerald, G. M. Frick, R. E. Larson, and E. J. Mack, Aerosol size and optical properties found in the marine boundary layer over the Atlantic Ocean, *J. Geophys. Res.*, **95**, 3659-3686, 1990.
- Intergovernmental Panel on Climate Change (IPCC), Radiative forcing of climate change, in *The Science of Climate Change*, edited by J. T. Houghton et al., pp. 65-132, Cambridge Univ. Press, New York, 1996.

- Jaenicke, R., Tropospheric aerosols in *Aerosol-Cloud-Climate Interactions*, edited by P. V. Hobbs, pp. 1-31, San Diego, Calif., 1993.
- Kaufman, Y. J., D. Tanré, H. R. Gordon, T. Nakajima, J. Lenoble, R. Frouin, H. Grassl, B. M. Herman, M. D. King, and P. M. Teillet, Passive remote sensing of tropospheric aerosol and atmospheric correction for the aerosol effect, *J. Geophys. Res.*, **102**, 16,815-16,830, 1997.
- Kim, Y., H. Sievering, J. Boatman, D. Wellman, and A. Pszenny, Aerosol size distribution and aerosol water content measurements during Atlantic Stratocumulus Transition Experiment/Marine Aerosol Gas Exchange, *J. Geophys. Res.*, **100**, 23,027-23,038, 1995.
- Klett, J. D., Stable analytical inversion solution for processing lidar return, *Appl. Opt.*, **20**, 211-220, 1981.
- Klett, J. D., Lidar inversion with variable backscatter/extinction ratios, *Appl. Opt.*, **24**, 1638-1643, 1985.
- Kovalev, V. A., Sensitivity of the lidar solution to errors of the aerosol backscatter to extinction ratio: influence of a monotonic change in the aerosol extinction coefficient, *Appl. Opt.*, **34**, 18, 3457-3462, 1995.
- Measures, R. M., *Laser Remote Sensing*, 510 pp., Wiley Intersci., New York, 1984.
- Melfi, S. H., J. D. Sphinirne, S. H. Chou, and S. P. Palm, Lidar observations of the vertically organised convection in the planetary boundary layer over the ocean, *J. Clim. Appl. Meteorol.*, **24**, 806-821, 1985.
- Menzies, R. T., D. M. Tratt, and P. H. Flamant, Airborne CO₂ coherent lidar measurements of cloud backscatter and opacity over the ocean surface, *J. Atmos. Oceanic Technol.*, **11**, 770-778, 1994.
- Menzies, R. T., Lidar In-Space Technology Experiment (LITE) measurements of ocean surface directional reflectance and wind speed, paper presented at the National Oceanic and Atmospheric Administration Work Group on Space-Based Lidar Winds, San Francisco, Calif., July 1995.
- Monahan, E. C., E. D. Spiel, and K. L. Davidson, A model of marine aerosol generation via whitecaps and wave disruption, in *Oceanic Whitecaps and Their Role in Air-Sea Exchange Processes*, edited by E. C. Monahan and G. MacNiocaill, pp. 167-174, Reidel, Norwell, Mass., 1986.
- Morel, A., and L. Prieur, Analysis of variations of ocean color, *Limnol. Oceanogr.*, **22**, 709-722, 1977.
- O'Dowd, C. D., M. E. Smith, I. E. Consterdine, and J. A. Lowe, Marine aerosol, sea-salt and the marine sulphure cycle: A short review, *Atmos. Environ.*, **1**, 73-80, 1997.
- Park, P. M., M. H. Smith, and H. J. Exton, The effect of mixing height on maritime aerosol concentrations over the North Atlantic Ocean, *Q. J. R. Meteorol. Soc.*, **116**, 461-476, 1990.
- Petri, K. J., Laser radar reflectance of Chesapeake Bay Waters as a function of wind speed, *IEEE Trans. Geosci. Electron.*, **GE-15**, 87-96, 1977.
- Ramonet, M., and P. Monfray, Selection of baseline conditions in a 3D atmospheric transport model: application to the seasonal and synoptic variations of CO₂, *Tellus, Ser. B*, **48**, 502-520, 1996.
- Reagan, J. A., and D. A. Zielinskie, Spaceborne lidar remote sensing techniques aided by surface returns, *Opt. Eng.*, **30**, 96-101, 1991.
- Russel, L. M., S. N. Pandis, and J. H. Seinfeld, Aerosol production and growth in the marine boundary layer, *J. Geophys. Res.*, **99**, 20,989-21,003, 1994.
- Shettle, E. P., and R. W. Fenn, Models for the aerosols of the lower atmosphere and the effects of humidity variations on their optical properties, *AFGL Rep. TR-79-0214*, Air Force Geophys. Lab., Bedford, Mass., 1979.
- Smith, M. H., I. E. Consterdine, and P. M. Park, Atmospheric loadings of marine aerosol during a Hebridean cyclone, *Q. J. R. Meteorol. Soc.*, **115**, 383-395, 1989.
- Smith, M. H., P. M. Park, and I. E. Consterdine, Marine aerosol concentrations and estimated fluxes over the sea, *Q. J. R. Meteorol. Soc.*, **119**, 809-824, 1993.
- Spinhirne, J. D., and W. D. Hart, Cirrus structure and radiative parameters from airborne lidar and spectral radiometer observations: The 28 October 1986 FIRE study, *Mon. Weather. Rev.*, **118**, 2329-2343, 1990.
- Spinhirne, J. D., J. A. Reagan, and B. M. Herman, Vertical distribution of aerosol extinction cross section and inference of aerosol imaginary index in the troposphere by lidar technique, *J. Appl. Meteorol.*, **19**, 426-438, 1980.
- Strawbridge, K. B., and R. M. Hoff, LITE validation experiment along California's coast: Preliminary results, *Geophys. Res. Lett.*, **23**, 73-76, 1996.
- Weill, A., et al., SOFIA 1992 experiment during ASTEX, *The Global Atmosphere and Ocean System*, **3**, 355-395, 1995.
- Weinman, J. A., Derivation of atmospheric extinction profiles and wind speed over the ocean from a satellite-borne lidar, *Appl. Opt.*, **27**, 3994-4001, 1988.
- Winker, D.M., R. H. Couch, and M. P. McCormick, An overview of LITE: NASA's Lidar In-Space Technology Experiment, *Proc. IEEE*, **84**, 164-180, 1996.

C. Flamant, V. Trouillet and J. Pelon, Service d'Aéronomie du CNRS, Université Pierre et Marie Curie, Tour 15, Boite 102, 4 Place Jussieu, 75252 Paris Cedex 05, France. (e-mail: cyf@aero.jussieu.fr; vit@aero.jussieu.fr; jpe@aero.jussieu.fr)

P. Chazette, Laboratoire des Sciences du Climat et de l'Environnement du CEA/CNRS, Orme des Merisiers, 91191 Gif-sur-Yvette Cedex, France. (e-mail: pch@lsce.saclay.cea.fr)

(Received March 26, 1997; revised July 2, 1998; accepted July 8, 1998.)